

**Editor Comments:**

The authors have thoroughly and satisfactorily responded to the suggestions and comments by the reviewers. Hence I am glad to accept this manuscript for publication in Climate of the Past.

Before final publication I would like the authors to reconsider a minor, but potentially misleading formulation. The authors state in their conclusion (lines 701, 702) that "the simulations provide insights into key dynamics features of the transition, ..." Time slice simulations cannot, in principle, address the dynamics of the transition of the climate system as pointed out by reviewer 1. They can however, as correctly replied by the authors, provide insights into different climate states, i.e. modes of operation, or dynamics, of the atmosphere and the ocean, during the transition. I ask the authors for modifying their formulation.

**Thank you for the opportunity to revise this section to avoid confusion. We changed our final paragraph in the conclusion from:**

The eight time slice simulations depict the glacial-interglacial transition that is in good agreement with other AOGCM simulations and compares reasonably well with data-based climate reconstructions. The simulations provide insights into key dynamic features of the transition, such as altered NH storm tracks and strengthening of monsoons during the early to mid-Holocene. The data-model and model-model comparisons give us a measure of confidence that our paleo GENMOM simulations are reasonable on broad spatial scales and adds to the growing number of climate models that are capable of simulating key aspects of past climate change when constrained by a relatively small set of global boundary conditions. Future work using the model output produced by this study will address how internal model variability and multidecadal variability influence comparison with proxy data, particularly in North America using dynamical downscaling techniques.

**To:**

The eight time slice simulations depict the glacial-interglacial transition that is in good agreement with other AOGCM simulations and compares reasonably well with data-based climate reconstructions. The data-model and model-model comparisons give us a measure of confidence that our paleo GENMOM simulations are reasonable on broad spatial scales and adds to the growing number of climate models that are capable of simulating key aspects of past climate change when constrained by a relatively small set of global boundary conditions. While our simulations are not continuous across the deglaciation and do not include events such as freshwater forcing, they do provide insights into between period changes, such as altered NH storm tracks and strengthening of monsoons during the early to mid-Holocene and multi-century time series that are useful, for example, to explore ecosystem responses to changes in mean climate and the related interannual variability in the model. Future work using the model output produced by this study will address

how internal model variability and multidecadal variability influence comparison with proxy data, particularly in North America using dynamical downscaling techniques.

1

2

3 Global climate simulations at 3,000-year intervals for the last 21,000 years  
4 with the GENMOM coupled atmosphere-ocean model

5

6 J. R. Alder and S. W. Hostetler

7

8 Jay R. Alder, US Geological Survey, College of Earth, Ocean and Atmospheric Sciences,  
9 Oregon State University, Corvallis, Oregon 97331, United States, [jalder@usgs.gov](mailto:jalder@usgs.gov)

10

11 Steven W. Hostetler, US Geological Survey, College of Earth, Ocean and Atmospheric  
12 Sciences, Oregon State University, Corvallis, Oregon 97331, United States,  
13 [swhostet@usgs.gov](mailto:swhostet@usgs.gov)

14

15

16

17

18

19

20

21

22

23

24

25

26

27

28

29

30

31

---

32 Corresponding author address: Jay Alder  
33 E-mail: [jalder@usgs.gov](mailto:jalder@usgs.gov)

34

35

35 **Abstract**

36 We apply GENMOM, a coupled atmosphere-ocean climate model, to simulate  
37 eight equilibrium time slices at 3000-yr intervals for the past 21,000 years forced by  
38 changes in Earth-Sun geometry, atmospheric greenhouse gases (GHGs), continental ice  
39 sheets and sea level. Simulated global cooling during the Last Glacial Maximum (LGM)  
40 is 3.8 °C and the rate of post-glacial warming is in overall agreement with recently  
41 published temperature reconstructions. The greatest rate of warming occurs between 15  
42 and 12 ka (2.4 °C over land, 0.7 °C over oceans and 1.4 °C globally) in response to  
43 changes in radiative forcing from the diminished extent of the Northern Hemisphere  
44 (NH) ice sheets and increases in GHGs and NH summer insolation. The modeled LGM  
45 and 6 ka temperature and precipitation climatologies are generally consistent with proxy  
46 reconstructions, the PMIP2 and PMIP3 simulations, and other paleoclimate data-model  
47 analyses. The model does not capture the mid-Holocene ‘thermal maximum’ and gradual  
48 cooling to pre-industrial global temperature found in the data. Simulated monsoonal  
49 precipitation in North Africa peaks between 12 and 9 ka at values ~50% greater than  
50 those of the PI, and Indian monsoonal precipitation peaks at 12 and 9 ka at values ~45%  
51 greater than the PI. GENMOM captures the reconstructed LGM extent of NH and  
52 Southern Hemisphere (SH) sea ice. The simulated present-day Antarctica Circumpolar  
53 Current (ACC) is ~48% weaker than the observed (62 versus 119 Sv). The simulated  
54 present-day Atlantic Meridional Overturning Circulation (AMOC) of  $19.3 \pm 1.4$  Sv on  
55 the Bermuda Rise (33°N) is comparable with observed value of  $18.7 \pm 4.8$  Sv. AMOC at  
56 33°N is reduced by ~15% during the LGM, and the largest post-glacial increase (~11%)  
57 occurs during the 15 ka time slice.

58 **1 Introduction**

59 The history of the climate system over the past 21,000 years reflects the combined  
60 changes in earth-sun orbital geometry, atmospheric greenhouse gas concentrations  
61 (GHG), the extent of the Northern Hemisphere (NH) ice sheets, and sea level. GHG  
62 levels were lowest during the Last Glacial Maximum (LGM, ~21,000 years ago, 21 ka)  
63 and increased thereafter to pre-industrial (PI) levels (Brook et al., 2000; Monnin et al.,  
64 2001; Sowers et al., 2003). The LGM is further characterized by the large Laurentide  
65 (LIS), Cordilleran (CIS) and Fennoscandian (FIS) ice sheets. The height and extent of the  
66 ice sheets altered atmospheric circulation patterns, and the extent increased the NH  
67 albedo thereby altering the global radiative balance. The effect of the ice sheets on  
68 climate progressively diminished from the LGM to the early Holocene as global warming  
69 driven by increasing GHGs combined with changes in NH summer insolation to  
70 accelerate ice sheet ablation. Abrupt departures from the comparatively smooth transition  
71 from the LGM through the Holocene, such as Heinrich and Dansgaard-Oeschger events,  
72 the Bølling-Allerød (BA), and the Younger Dryas (YD), are evident in geologic records,  
73 and these events likely influenced the overall trajectory of the deglaciation.

74 The climate of the past 21,000 years has been studied extensively, beginning with  
75 three international collaborative projects: the Long range Investigation, Mapping, and  
76 Prediction (CLIMAP; CLIMAP Project Members, 1981) and the Cooperative Holocene  
77 Mapping Project (COHMAP; COHMAP Members, 1988), which evolved into the  
78 Testing Earth System Models with Paleoenvironmental Observations (TEMPO) project  
79 (Kutzbach et al., 1996a; 1998). CLIMAP focused on reconstructing the LGM climate,  
80 COHMAP focused on reconstructing the climate of seven time periods (18, 15, 12, 9, 6, 3

81 ka), and TEMPO focused on reconstructing the climate of 21, 16, 14, 11 and 6 ka. These  
82 three projects pioneered data-model comparison through integrating climate model  
83 simulations and paleoclimatic data, which motivated the development of new techniques  
84 for analyzing geologic data and led to improvements in general circulation models.

85 More recently, the Palaeoclimate Modelling Intercomparison Project (PMIP) is  
86 actively working to advance reconstruction of LGM and 6 ka climate through  
87 model-to-model evaluations and data-model comparisons. PMIP has now entered the  
88 third phase (PMIP3; Braconnot et al., 2012) and is a component of phase 5 of the Climate  
89 Model Intercomparison Project (CMIP5). In contrast to CLIMAP, COHMAP, TEMPO  
90 and earlier PMIP model experiments that employed fixed sea surface temperatures (SST)  
91 and mixed-layer ocean models, some of the PMIP2 experiments and all of the PMIP3  
92 experiments include fully coupled ocean and atmospheric models. Braconnot et al. (2012)  
93 review some of the highlights of the PMIP2 experiments and the design of the PMIP3  
94 experiments and Harrison et al. (2013) evaluate the PMIP3 and PMIP2 simulations of  
95 LGM and 6 ka climates with data-model comparisons. In addition, continuous  
96 simulations of climate over the last 21 ka have been achieved with earth system models  
97 of intermediate complexity (e.g., Timm and Timmermann, 2007), and the TraCE-21ka  
98 project at the National Center for Atmospheric Research (NCAR) conducted continuous,  
99 transient climate simulations from 22 ka to 6.5 ka with the coupled NCAR Community  
100 Climate System Model (Liu et al., 2009). Singarayer and Valdes (2010) simulated the  
101 climate of the last 120,000 years using model snapshots at 4 ka and 1 ka intervals.

102 Here we explore past changes in late-Pleistocene climate using the coupled  
103 Atmosphere-Ocean General Circulation Model (AOGCM) GENMOM. We simulated

104 multi-century time slices that span the interval from LGM to pre-industrial (PI) every  
105 three thousand years (21, 18, 15, 12, 9, 6, 3 ka and PI). The simulations were run with  
106 prescribed insolation, GHG concentrations, continental ice sheets, land extent and sea  
107 level as boundary conditions. We analyze the within and between climatology of the time  
108 slices and compare the 21 ka and 6 ka results with terrestrial and marine climate  
109 reconstructions and results from the PMIP2 and PMIP3 simulations. The goal of our  
110 simulations is to adopt a methodological framework similar to that of PMIP to simulate  
111 time slices between the LGM and mid-Holocene. The simulations also serve as a base  
112 line for applying GENMOM to more detailed and focused studies of late-Pleistocene  
113 climate such as quantifying the effects of freshwater forcing and dynamic vegetation  
114 feedbacks.

## 115 2 Methods

### 116 2.1 Model description

117 GENMOM combines version 3 of the GENESIS atmospheric model (Pollard and  
118 Thompson, 1997; Thompson and Pollard, 1995; 1997) with version 2 of the Modular  
119 Ocean Model (MOM2, Pacanowski, 1996). Version 3 of GENESIS (Alder et al., 2011;  
120 Kump and Pollard, 2008; Pollard and Thompson, 1997; Zhou et al., 2008) incorporates  
121 the NCAR CCM3 radiation code (Kiehl et al., 1998). GENESIS has been developed with  
122 an emphasis on representing terrestrial physical and biophysical processes, and for  
123 application to paleoclimate experiments. Earlier versions of GENESIS (Pollard and  
124 Thompson, 1994; 1995; 1997; Thompson and Pollard, 1995; 1997) have been applied in  
125 a wide range of modern and paleoclimate studies (Beckmann et al., 2005; Bice et al.,  
126 2006; DeConto et al., 2007; 2008; Horton et al., 2007; Hostetler et al., 2006; Miller et al.,

127 2005; Poulsen et al., 2007a; 2007b; Ruddiman et al., 2005; Tabor et al., 2014), and  
128 GENESIS simulations with fixed and slab ocean SSTs were included in PMIP1  
129 (Joussaume et al., 1999; Pinot et al., 1999; Pollard et al., 1998).

130 In our simulations, we employ a coupled model with T31 spectral truncation,  
131 which corresponds to a grid of 96 longitudes ( $3.75^{\circ}$ ) by 48 Gaussian latitudes ( $\sim 3.71^{\circ}$ ).  
132 The atmosphere is represented by 18 vertical sigma levels with mid-layers ranging from  
133 0.993 at the surface to 0.005 at the tropopause. GENESIS includes the Land Surface  
134 eXchange model, LSX, (Pollard and Thompson, 1995) to simulate surface processes and  
135 to account for the exchange of energy, mass and momentum between the land surface and  
136 the atmospheric boundary layer. MOM2 has 20 fixed-depth vertical levels and is  
137 implemented on essentially the same T31 horizontal grid as GENESIS through cosine-  
138 weighted distortion (Pacanowski, 1996). Sea ice is simulated by a three-layer model that  
139 accounts for local melting, freezing, and fractional cover (Harvey, 1988; Semtner, 1976)  
140 and includes the dynamics associated with wind and ocean current using the cavitating-  
141 fluid model of Flato and Hibler (1992). The atmospheric and ocean models interact every  
142 six hours without flux corrections.

143 GENMOM reproduces observed global circulation patterns, such as the seasonal  
144 change in the position and strength of the jetstreams and the major semi-permanent sea  
145 level pressure centers (Alder et al., 2011). The simulated present-day (PD) 2-m air  
146 temperature climatology (Table 1) is  $0.8^{\circ}\text{C}$  colder than observations globally,  $0.7^{\circ}\text{C}$   
147 colder over oceans, and  $0.9^{\circ}\text{C}$  colder over land. Similar to other AOGCMs (e.g., Lee and  
148 Wang, 2014), GENMOM produces a split ITCZ over the equatorial Pacific Ocean.

149 The pre-industrial Atlantic Meridional Overturning Circulation (AMOC)  
150 simulated by GENMOM is  $19.3 \pm 1.4$  Sv, which is stronger than, but comparable to, the  
151 observed value of 17.4 Sv (Srokosz et al., 2012). Simulated SSTs display a warm bias in  
152 some regions of the Southern Ocean, primarily south of 50°S around Antarctica, and a  
153 warm bias exceeding  $\sim 2$  °C between 200–1000 m depth in parts of the tropics and mid-  
154 latitudes. Alder et al. (2011) note that the warm bias in the Southern Ocean is associated  
155 with the relatively weak Antarctic Circumpolar Current (ACC) in GENMOM (62 Sv  
156 versus the observed value of 119 Sv) and Deacon Cell upwelling which allows excessive  
157 vertical mixing in the present-day GENMOM simulation, and together reduce sea ice  
158 around Antarctica, particularly during summer. Both of these features are present to some  
159 extent in our suite of simulations. We tested the Gent-McWilliams vertical ocean mixing  
160 scheme (Gent and McWilliams, 1990) in GENMOM but it did not improve the Southern  
161 Ocean warm bias, so we did not implement it in our paleosimulations.

162 The climate sensitivity of GENMOM for a doubling of CO<sub>2</sub> from present day is  
163 2.2 °C, which is in the lower range of other coupled AOGCMs (Meehl et al., 2007) and is  
164 consistent with recent estimates of 2.7 °C based on the PMIP3 LGM simulations  
165 (Harrison et al., 2013) and paleodata-model estimates of 2.8 °C (Annan and Hargreaves,  
166 2013) and 2.3 °C (Schmittner et al., 2011b).

167 Reflecting lower GHG concentrations, the average NH 2-m temperature in our PI  
168 simulation is 0.79 °C cooler than our PD simulation, where as the PD simulation is 1.97  
169 °C cooler than observations and reflects the lower GHG concentrations specified in the PI  
170 simulation (Tables 1 and 2). The PI-to-PD warming in the NH is similar to the observed  
171 warming of  $\sim 0.6 - 0.9$  °C (Brohan et al., 2006) and is in the range of response of other

172 climate models (e.g., Otto-Bliesner et al., 2006b). The greatest regional warming between  
173 the in the PD simulation (not shown) is  $\sim 3$   $^{\circ}\text{C}$  over the high northern latitudes and  
174 northern polar regions during boreal autumn, winter and spring, consistent with the  
175 observed polar amplification (Hassol, 2004).

176 **2.2 Experimental design**

177 We applied GENMOM to eight time periods for 21, 18, 15, 12, 9, 6, 3 ka and pre-  
178 industrial. We prescribed insolation at the top of atmosphere for each time slice (Fig. 1)  
179 by specifying appropriate orbital parameter values for precession, obliquity and  
180 eccentricity (Table 1, Berger and Loutre, 1991). The solar constant was set to  $1367 \text{ W m}^{-2}$   
181 for all time periods. We estimated GHG concentrations from ice-core records by applying  
182 a  $\pm 300$  yr averaging window centered on the time period of interest (Table 1), and we  
183 specified the PMIP3 GHG concentrations for our PI simulation (Braconnot et al., 2007a).

184 To derive continental ice sheets for the time slices, we used the ICE-4G  
185 reconstructions (Peltier, 2002) for the Fennoscandian (FIS) and Cordilleran (CIS), and  
186 the Oregon State University Laurentide Ice Sheet (OSU-LIS) reconstruction (Hostetler et  
187 al., 1999; Licciardi et al., 1998) (Fig. 2). The ICE-6G reconstruction was not available for  
188 our 8 time slices at time we began our simulations. However, the OSU-LIS  
189 reconstruction has similar ice sheet topography to that of ICE-6G (Ullman et al., 2014)  
190 and was available for our simulation periods. The combination of OSU-LIS and ICE-4G  
191 enables us to use a more realistic LIS topography than that of ICE-5G, particularly over  
192 the LIS during the deglacial, and facilitates adjusting sea level throughout our time slices.  
193 A similar ice sheet configuration (OSU-LIS and ICE5-G) was used as a boundary  
194 condition in the NASA GISS-E2-R LGM simulation submitted to the PMIP3 archive

195 (Ullman et al., 2014). We specified the 10 ka OSU-LIS ice sheet to ensure that Hudson  
196 Bay remained covered by the LIS at 9 ka (Dyke and Prest, 1987). The ICE-4G  
197 reconstruction includes an Eastern Siberian Ice Sheet, which we removed because it did  
198 not exist (Felzer, 2001).

199 Topographic heights of the land masses were altered to reflect relative sea-level  
200 change in ICE-4G. We created the topography and land mask for each time slice by  
201 applying orographic changes to the present-day Scripps global orography data set (Gates  
202 and Nelson, 1975). Orographic changes based on ICE-4G exposed or flooded land grid  
203 cells associated with relative sea level (e.g. Indonesia, Papua New Guinea). We set the  
204 ocean bathymetry to modern depths for ocean grid cells.

205 We specified the modern distribution of vegetation (Dorman and Sellers, 1989)  
206 for all simulations because reconstructions of global vegetation for all time slices either  
207 do not exist or are not well constrained. We note that while setting vegetation to modern  
208 distribution for all simulations isolates the period-to-period climate response to other  
209 boundary conditions, we do not capture dynamic vegetation-climate feedbacks that may  
210 be important in some regions such as North Africa (Kutzbach et al., 1996b; Timm et al.,  
211 2010) and the high latitudes of the NH (Claussen, 2009; Renssen et al., 2004). The  
212 vegetation type on emergent land cells is set to be the same as neighboring existing land  
213 cells. The simulations do not include varying dust forcing across the time slices, which  
214 may account for up to 20% of the radiative change (Köhler et al., 2010; Rohling et al.,  
215 2012). Freshwater flux from land-based precipitation is globally averaged and spread  
216 over the world ocean (Alder et al., 2011).

217 In accordance with the PMIP3 protocol, to conserve atmospheric mass we  
218 compensated for changes in global topography in each time slice by holding global  
219 average surface pressure constant. At T31 resolution the Bering Strait and the Strait of  
220 Gibraltar are closed in the default MOM2 bathymetry. We conducted sensitivity tests and  
221 adjusted the bathymetry to ensure that key passages (e.g. Drake Passage, Norwegian Sea,  
222 and Indonesian Throughflow) were adequately represented. Additional sensitivity testing  
223 revealed that the modeled AMOC and salinity of the Arctic are very sensitive to the  
224 bathymetry of the Norwegian Sea, particularly to the width of the passage between  
225 Scandinavia and Greenland as it narrowed by the growth of the FIS. We removed Iceland  
226 from the model to ensure that the passage remained sufficiently wide and deep to prevent  
227 unrealistic buildup of salinity in the Arctic.

228 Each time slice simulation was initialized from a cold start (isothermal  
229 atmosphere, latitudinally dependent ocean temperature profile, and uniform salinity of 35  
230 ppt) and run for 1,100 years. We exclude the first 1,000 years from our analysis here to  
231 allow for spin up of ocean temperatures. The temperature drift in the last 300 years of our  
232 simulations (SFig. 1) is acceptably small (Braconnot et al., 2007a; Singarayer and Valdes,  
233 2010) with values of -0.05 °C/century for the LGM, 0.01 °C/century for 6 ka, and -0.02  
234 °C/century for PI. Drift in the LGM and early deglacial simulation is attributed primarily  
235 to long-term cooling and the evolution of sea ice in the southern ocean. Simulated  
236 AMOC exhibits decadal scale variability, but was free of drift over the last 300 years of  
237 the simulations.

238 In what follows, the monthly averages of the model output are based on the  
239 modern calendar as opposed to the angular calendar that changes with Earth-sun

240 geometry (Pollard and Reusch, 2002; Timm et al., 2008). The modern calendar is  
241 commonly used in data-model comparisons (e.g., Harrison, 2013).

242 **3 Results**

243 **3.1 Atmospheric circulation**

244 The boreal winter (DJF) 500 hPa heights in the PI simulation (Fig. 3a) display the  
245 observed high- and mid-latitude ridge-trough-ridge-trough standing wave structure (wave  
246 number two) that arises from continent-ocean-continent-ocean geography of the NH  
247 (Peixoto and Oort, 1992). From 21 ka to 9 ka the LIS, the FIS and Greenland ice sheets  
248 alter the NH standing wave structure resulting in persistent, distinct troughs and cyclonic  
249 flow tendencies over northeast Asia, the North Pacific, the continental interior of North  
250 America, the North Atlantic and Europe (Fig. 3, maps of raw fields SFig. 2).

251 Consistent with previous LGM studies using comparable (Braconnot et al., 2007a)  
252 and higher-resolution (Kim et al., 2007; Untermaier et al., 2011) climate models, from 21  
253 ka through 9 ka the western edge of the Cordilleran Ice Sheet diverts the LGM winter  
254 polar jetstream resulting in one branch that is weaker than PI over the Gulf of Alaska and  
255 the western and central regions of the ice sheet, and a second branch to the south of the  
256 ice sheet that is stronger than the PI (Fig. 3a). The reorganization creates westward wind  
257 anomalies over the North American Pacific Northwest. The LIS effectively guides the  
258 convergence of the branches, and the meridional gradient of low and high 500 hPa height  
259 anomalies in the North Atlantic intensifies flow over North America, the North Atlantic,  
260 Europe and Northern Africa (Figs. 3a) thereby altering the path of storm tracks. This flow  
261 pattern weakens progressively as the LIS recedes.

262 The influence of the NH ice sheets is also evident in summer (JJA), but to a lesser  
263 degree than in winter (Fig. 3b) due to continental heating and the absence of the strong,  
264 mid-latitude storm tracks. Between 21 ka and 15 ka, the summer jetstream is constrained  
265 and therefore enhanced along and to the south of the southern margin of the LIS  
266 extending over the North Atlantic. At 18 ka, a trend toward positive JJA anomalies in 500  
267 hPa heights emerges over the regions of the semi-permanent subtropical high pressure of  
268 the North Pacific and central Atlantic. The regions of positive height anomalies, and their  
269 associated anticyclonic wind anomalies, expand over central North America, peak from  
270 12 ka through 9 ka, and diminish by 6 ka (Fig. 3). The DJF pattern of low-to-high height  
271 anomalies over the North Atlantic is replaced during JJA by a strengthened subtropical  
272 high. Anticyclonic flow around positive height anomalies on the western edge of the FIS  
273 alters regional flow patterns over and south of the ice sheet. The GENMOM responses to  
274 the NH ice sheets are similar to many previous modeling experiments that have  
275 established that changes in tropospheric pressure–surface heights and winds are primarily  
276 driven by changes in ice-sheet height, and secondarily by temperature and albedo  
277 feedbacks (COHMAP Members, 1988; Felzer et al., 1996; 1998; Otto-Bliesner et al.,  
278 2006a; Pausata et al., 2011; Pollard and Thompson, 1997; Rind, 1987).

279 From 21 ka to 12 ka, the largest changes in boreal winter sea-level pressure (SLP)  
280 are associated with negative surface temperature anomalies over the continental ice  
281 sheets, the landmasses of the NH, and areas of expanded sea ice in the North Atlantic  
282 (Fig. 4a) where cooling increases subsidence and thus contributes to cold high surface  
283 pressure. From 21 ka to 15 ka, high pressure over the LIS produces anticyclonic flow  
284 across the northern Great Plains and over the Puget Lowlands of the US. Similar

285 anticyclonic tendencies are simulated along the margin of the FIS. Between 12 ka and 6  
286 ka the winter SLP around the Aleutian low in the North Pacific and the Icelandic low in  
287 the North Atlantic is strengthened relative to PI. The Aleutian low is expanded southward  
288 whereas the Icelandic low is confined on the northern edge by the FIS and is slightly  
289 displaced southeastward.

290 From 21 ka to 9 ka, the JJA SLP anomalies remain strongly positive over the ice  
291 sheets and sea ice, whereas from 12 ka to 6 ka the SLP anomalies over Northern  
292 Hemisphere landmasses are negative due to enhanced continental warming (Fig. 4b). The  
293 patterns of the JJA 500 hPa heights, SLP and the associated circulation over North  
294 America and adjacent oceans again illustrate similar responses to time-varying controls:  
295 changes from 21 ka to 15 ka are primarily driven by changes in the LIS, whereas from 12  
296 ka to 6 ka the circulation changes are related to the changes in the seasonality of  
297 Holocene NH insolation (Fig. 2).

298 **3.2 Near-surface air temperature**

299 Our time slice simulations clearly display surface air temperature (SAT) changes  
300 attributed to radiative forcing from the presence of the continental ice sheets, GHGs  
301 (Clark et al., 2012), and insolation (Fig. 5). The global average mean annual LGM  
302 temperature simulated by GENMOM is 3.8 °C colder than the PI (Table 2, Fig. 5a),  
303 within the range of cooling in the PMIP2 AOGCM simulations (3.1 °C to 5.6 °C and  
304 average 4.4 °C) and the PMIP3 simulations (2.6 °C to 5.0 °C and average of 4.4 °C) that  
305 were forced by similar boundary conditions (Harrison et al., 2013; Kageyama et al.,  
306 2006). Our LGM cooling is also in agreement with Annan and Hargreaves (2013), who  
307 reconciled the PMIP2 ensemble and proxy data to derive an estimated cooling of  $4.0 \pm$

308 0.8 °C, but falls outside the range of Schmittner et al. (2011b) who found a median  
309 cooling of 3.0 °C (66% probability range of 2.1 °C - 3.3 °C). GENMOM is also consistent  
310 with three transient simulations (Liu et al., 2014) averaged over the periods simulated by  
311 GENMOM. Excluding the BA and YD, our simulations reproduce the rate of warming  
312 between 21 ka and 15 ka, but are consistently ~1 °C colder than the reconstruction of  
313 Shakun et al. (2012) when sampled at the proxy sites (Fig. 5b). During these periods,  
314 GENMOM falls at the low end or outside the range of the transient models; however,  
315 GENMOM falls within the range of LGM and MH cooling simulated by the PMIP3  
316 models, which have similar experimental designs and large scale boundary conditions.

317 Neither GENMOM nor the ensemble mean of the PMIP3 models capture the  
318 ~0.5 °C the 6 ka temperature anomaly in the Marcott et al. (2013) reconstruction. The  
319 change in the 6 ka mean annual temperature at the proxy sites in the 12 PMIP3 models  
320 we analyzed ranged from -0.3 to 0.3 °C with a mean of ~0.0 °C. Three models simulated  
321 slight warming, five near zero and four simulated slight cooling. Whether or not some  
322 proxies used in the temperature reconstructions have seasonal bias which would  
323 exaggerate the mid-Holocene warming remains an open research question (Liu et al.,  
324 2014).

325 Seasonal temperature changes across our time slice simulations illustrate the  
326 spatial and temporal effect of changing boundary conditions (Fig. 6). From 21 ka through  
327 15 ka, both DJF and JJA exhibit cold temperature anomalies exceeding 16 °C over and  
328 adjacent to the ice sheets in both hemispheres. With the exception of Europe and the high  
329 latitudes of the NH, boreal winters remain generally colder than PI over the continents  
330 until 3 ka (Fig. 6), corresponding to reduced insolation. NH atmospheric circulation

331 changes induced by atmospheric blocking from the LIS (Fig. 3) sustain positive winter  
332 and summer temperature anomalies over Beringia. Summer warming also occurs south of  
333 the FIS across much of Asia. Although the mid-Holocene wintertime deficit in insolation  
334 is small at high northern latitudes, changes in short-wave radiation at the surface during  
335 boreal summer in the model are large and positive ( $30 - 40 \text{ Wm}^{-2}$ ) due to the precessional  
336 shift of perihelion and changes in obliquity (SFig. 4). Substantial warming occurs  
337 between most pairs of consecutive time slices from the LGM through the Holocene (Fig.  
338 7, Table 2); however, over the African and Indian monsoon regions increased cloudiness  
339 associated with enhanced summer monsoonal precipitation leads to cooling from 15 to 6  
340 ka.

341 The relatively high rate of warming between 18 ka and 15 ka ( $1.5 \text{ }^{\circ}\text{C}$  land and  
342  $0.5 \text{ }^{\circ}\text{C}$  ocean, Fig. 7, Table 2) is commensurate with increased GHGs (Table 1). Periods  
343 of peak annual warming from 15 ka to 12 ka ( $2.4 \text{ }^{\circ}\text{C}$  land and  $0.7 \text{ }^{\circ}\text{C}$  ocean) and from 12  
344 ka to 9 ka ( $1.6 \text{ }^{\circ}\text{C}$  land and  $0.2 \text{ }^{\circ}\text{C}$  ocean) are associated with increasing GHG  
345 concentrations, ablation of the NH ice sheets (Figs. 1 and 6a). The simulated rates of  
346 annual global warming between the LGM and the early Holocene (Fig. 5) are in  
347 agreement with data (Clark et al., 2012; Gasse, 2000), and the analyses by Shakun et al.  
348 (2012) and Marcott et al. (2013) who attribute a large component of the warming to rising  
349 GHG levels.

350 The DJF and JJA temperature differences in our 21 ka simulation are similar to  
351 those of the PMIP3, allowing for differences in between our prescribed NH ice sheets  
352 (ICE-4G+OSU-LIS in GENMOM) and the blended ice sheet of the PMIP3 simulations  
353 that essentially combines the height of the ICE6G reconstruction with the extent of the

354 Dyke and Prest (1987) reconstructions (SFigs. 5 - 10, Braconnot et al., 2012). In both  
355 seasons, GENMOM produces 0.5 - 1 °C less cooling in the tropical oceans and greater  
356 warming over Beringia. The positive JJA temperature anomaly south of the FIS in  
357 GENMOM persists through 15 ka. Summer warming in the presence of the ice sheet was  
358 identified in earlier versions of GENESIS (Pollard and Thompson, 1997) and is  
359 associated with subsidence over the ice (Rind, 1987). Similar JJA warming also occurs in  
360 some of the PMIP3 models, but is likely a model artifact (Pollard and Thompson, 1997;  
361 Ramstein and Joussaume, 1995; Rind, 1987).

362 The DJF and JJA temperature anomalies in our 6 ka simulation are also similar to  
363 those of the PMIP3 models (SFigs. 7 and 8). Relative to PI, GENMOM produces slightly  
364 greater winter warming over Scandinavia than is evident in the average of the PMIP3  
365 simulations, and is generally 0.5 - 1.0 °C cooler over Asia, Africa and South America.  
366 During boreal summer, GENMOM simulates warming over the NH landmasses and  
367 cooling over the North African and Indian monsoon regions, consistent with the PMIP3  
368 models. Continental warming in GENMOM is ~ 0.5 - 1.0 °C weaker than most PMIP3  
369 models, particularly in Europe and Asia. A portion of the weaker warming in GENMOM  
370 is attributed to the prescribed 6 ka GHG concentrations we derived from the ice-core data  
371 that differ slightly from those specified for the PMIP3 experiments (Table 1 caption).

372 **3.3 Precipitation and monsoons**

373 The simulated global precipitation anomalies display a progression from the drier  
374 and colder conditions of the LGM to the warmer and wetter conditions of the Holocene  
375 (Fig. 8, Table 2). The global mean annual precipitation change of  $-0.29 \text{ mm d}^{-1}$  for the  
376 LGM is distributed as greater drying over land and ice sheets ( $-0.30 \text{ mm d}^{-1}$ ) than oceans

377 (-0.22 mm d<sup>-1</sup>). Regionally coherent patterns of precipitation change (Figs. 8 and 9) are  
378 indicative of displacement and changes in the strength of storm tracks (Li and Battisti,  
379 2008), the ITCZ and the Hadley circulation, and the onset, amplification and subsequent  
380 weakening of the global monsoons regions (Broccoli et al., 2006; Chiang, 2009; Chiang  
381 and Bitz, 2005).

382 Between the LGM and 15 ka, during DJF areas over and adjacent to the NH ice  
383 sheets display predominately reduced precipitation arising from a combination of the  
384 desertification-effect of the high and cold ice, lower-than-present atmospheric moisture  
385 and cloudiness and the advection of cold, dry air off of the ice sheets (Figs. 3a, 4a, 6a and  
386 8a). The topographic and thermal effects of the LIS and the thermal effect of sea ice

387 (Kageyama et al., 1999; Li and Battisti, 2008) alter 500 hPa geopotential heights  
388 along the southern margin of the ice sheet (Figs. 3a and SFig. 2a), causing the  
389 development of positive precipitation anomalies extending from the eastern Pacific across  
390 the Gulf of Mexico, eastern North America and into the Northern Atlantic.  
391 Accompanying negative precipitation anomalies over the North Atlantic and positive  
392 anomalies over the Nordic Seas are related to changes in the location of storm tracks. The  
393 local effect of the ice sheets on precipitation diminishes during the early and mid-  
394 Holocene as their influence on circulation weakens and the atmosphere becomes warmer  
395 and moister (Fig. 9a).

396 The negative DJF anomalies that persist from 21 ka to 15 ka during austral  
397 summer along the equatorial and low-latitude areas of South and Central America, south-  
398 central Africa Southeast Asia, Northern Australia, the tropical Atlantic, the Indian Ocean  
399 and the western Pacific warm pool are caused by changes in the location of the ITCZ and

400 weakened southern monsoonal circulation. This particularly affects the winter monsoon  
401 in central South America (Cheng et al., 2012; Zhao and Harrison, 2012) and in Southeast  
402 Asia and Indonesia where additional feedbacks in the energy and water balances over  
403 emergent land areas occur during low sea level stands (Figs. 1 and 8a) have been shown  
404 to alter the Walker Circulation (DiNezio and Tierney, 2013).

405 Precipitation for JJA also exhibits considerable change over time (Figs. 8b and  
406 9b). Similar to DJF, generally drier conditions are simulated over and adjacent to the NH  
407 ice sheets where anticyclonic flow tendencies suppress precipitation (Fig. 4b). Along  
408 portions of the southern margins of the LIS and FIS, however, orographic lifting  
409 enhances precipitation at 21 ka (Pollard and Thompson, 1997). Wetter conditions in the  
410 North American Southwest derive from enhanced westerly flow aloft and lower level  
411 southwesterly flow off the eastern Pacific that are associated with displacement of the  
412 jetstream by the ice sheets and the weakened Pacific subtropical high. Between 21 ka and  
413 12 ka the LIS causes an increased pressure gradient from a strengthened Azores-Bermuda  
414 high and weakened subtropical high in the eastern Pacific (Figs. 3b and 4b), resulting in  
415 amplified and displaced westward winds, drying over Central America, and wetter-than-  
416 present conditions over northern South America. At the LGM, North Africa, Europe, and  
417 all but the western edge of Asia, are drier than the PI, again reflecting the drier  
418 atmosphere of the full glacial.

419 The magnitude, gradients and spatial patterns of GENMOM 21 ka DJF  
420 precipitation anomalies are consistent with the PMIP3 experiments. Notable exceptions  
421 are greater drying than some models in the North Atlantic and the band of positive  
422 anomalies extending across the Gulf of Mexico and the southeast US. GENMOM

423 produces positive precipitation anomalies over Australia, which is present in four of the  
424 PMIP3 models. The 21 ka JJA precipitation anomalies are also in agreement with PMIP3,  
425 but display weaker drying over eastern NA and slight drying over the North Africa  
426 monsoon region.

427 The time evolution from LGM to PI of the African and Indian monsoons reflects  
428 the interplay of changes in the location of the ITCZ and Hadley circulation that are linked  
429 to the receding NH ice sheets, GHG-driven global warming, enhanced NH JJA insolation  
430 and changing land-SST temperature contrast. The North Africa and Indian monsoons are  
431 suppressed between 21 ka and 18 ka. After 18 ka, wetter-than-present conditions emerge  
432 in the monsoon regions of North Africa and India where increased JJA insolation warms  
433 the continents which amplifies the land-sea temperature contrasts that drive monsoonal  
434 circulation (Braconnot et al., 2007b; Kutzbach and Otto-Bliesner, 1982; Zhao and  
435 Harrison, 2012). The simulated DJF air temperatures in North Africa cool from the LGM  
436 until 15 ka, and then warm monotonically through the rest of the deglaciation and  
437 Holocene (Fig. 10). Wintertime precipitation over the North African region is minimal. In  
438 contrast, JJA temperatures increase throughout the deglaciation, peak at 9 ka, decrease  
439 slightly at 6 ka, and increase thereafter. A commensurate increase in JJA precipitation  
440 over North Africa between 12 ka and 6 ka is associated with northward migration of the  
441 ITCZ (Braconnot et al., 2007a; 2007b; Kutzbach and Liu, 1997), which enhances the  
442 transport of moisture into both the North African and Indian monsoon regions.  
443 Monsoonal precipitation peaks over both regions between 12 ka and 9 ka (Fig. 10). The  
444 change in precipitation between 9 ka and 6 ka over India ( $0.9 \text{ mm d}^{-1}$ ) is nearly double  
445 the change over North Africa ( $0.5 \text{ mm d}^{-1}$ ), consistent with the diagnoses of the mid-

446 Holocene monsoon of Marzin and Braconnot (2009) who attribute the stronger ~9 ka  
447 monsoon to insolation related to precession and snow cover on the Tibetan Plateau. The  
448 pattern of precipitation in the Indian monsoon region is similar to that of North Africa,  
449 but exhibits a greater range between peak Holocene values and the PI.

450 The overall temporal progression and magnitude of precipitation changes in the  
451 time slice simulations are in agreement with the PMIP2 (Braconnot et al., 2007a; 2007b)  
452 and PMIP3 simulations at 21 and 6 ka, and with other mid-Holocene modeling studies

453 (Hély et al., 2009; Kutzbach and Liu, 1997; Kutzbach and Otto-Bliesner, 1982;  
454 Timm et al., 2010). More specifically, the June through September GENMOM  
455 precipitation anomaly of  $-0.6 \text{ mm d}^{-1}$  over the North Africa monsoon region during the  
456 LGM is within the range ( $-0.9$  to  $0.1 \text{ mm d}^{-1}$ ) of 5 PMIP2 AOGCMs (Braconnot et al.,  
457 2007a) and 7 PMIP3 models (range of  $-0.6$  to  $0.2$  and average of  $-0.2 \text{ mm d}^{-1}$ ). The  
458 GENMOM LGM anomaly over India ( $-0.9 \text{ mm d}^{-1}$ ) is also within the range ( $-1.7$  to  $-0.1$   
459  $\text{mm d}^{-1}$ ) of the PMIP2 simulations (Braconnot et al., 2007a) and the PMIP3 simulations  
460 (range of  $-1.3$  to  $0.0$  and average of  $-0.7 \text{ mm d}^{-1}$ ).

461 The northward expansion and spatial pattern of precipitation anomalies of the 6 ka  
462 monsoons are in very good agreement with both the PMIP2 and PMIP3 experiments.  
463 Summer precipitation in the GENMOM simulation is enhanced by  $0.9 \text{ mm d}^{-1}$  relative to  
464 PI over North Africa, in agreement with the range ( $0.2$  to  $1.4 \text{ mm d}^{-1}$ ) and mean  
465 ( $0.7 \text{ mm d}^{-1}$ ) of 11 PMIP2 AOGCMs (Zhao and Harrison, 2012) and 12 PMIP3 models  
466 (range of  $0.1$  to  $1.0$  and average of  $0.6 \text{ mm d}^{-1}$ ). Over India, the 6 ka GENMOM  
467 precipitation anomaly of  $1.1 \text{ mm d}^{-1}$  exceeds the range ( $0.2$  to  $0.9 \text{ mm d}^{-1}$ ) and mean ( $0.6$

468 mm d<sup>-1</sup>) of the 11 PMIP2 models (Zhao and Harrison, 2012), but is within the range of  
469 the PMIP3 models (0.5 to 1.3 and average of 1.0 mm d<sup>-1</sup>).

470 **3.4 Sea ice**

471 DJF sea ice is present in the PI simulation over Hudson Bay, the Arctic Ocean,  
472 along the coast of eastern Canada, around Greenland, the Nordic Seas and the Baltic and  
473 North Sea (Fig. 11), in agreement with observed present-day distributions (Jaccard et al.,  
474 2005). Ice fractions of up to 100% are simulated over the Bering Sea and the Sea of  
475 Okhotsk. In the SH, sea ice persists through austral summer in the Weddell and Ross  
476 Seas and a few scattered locations around Antarctica. While the locations of the ice  
477 around Antarctica are in agreement with observations (Gersonde et al., 2005), the model  
478 underestimates the ice extent over the Weddell Sea and between the Weddell and Ross  
479 Seas. The lack of ice is partly attributable to a warm bias in the Southern Ocean  
480 associated with the previously mentioned weak ACC (discussed further below). During  
481 August and September, simulated sea ice is greatly reduced in the North Atlantic region  
482 (Fig. 11), with remnant ice persisting in the extreme north of Baffin Bay and the east  
483 coast of Greenland, also in agreement with observations. In the SH, the corresponding  
484 winter sea ice grows substantially and the distribution is in generally good agreement  
485 with observations (Gersonde et al., 2005).

486 The simulated annual average ice extents for the NH are  $9.8 \times 10^6$  km<sup>2</sup> for the  
487 LGM,  $15.8 \times 10^6$  km<sup>2</sup> for 6 ka and  $14.1 \times 10^6$  km<sup>2</sup> for PI (grid cells with fractional coverage  
488 > 15%). Compounded with climate-forcing, changes in both the distribution and areal  
489 coverage of the NH ice also reflect the change in ocean area due to the transition of land  
490 and ice sheets to ocean as sea level rises (Fig. 11 and SFigs. 13 - 15). For the same time

491 periods, the SH ice area extents, which are minimally affected by land-sea transitions with  
492 sea level rise, are  $20.9 \times 10^6 \text{ km}^2$ ,  $11.4 \times 10^6 \text{ km}^2$  and  $11.1 \times 10^6 \text{ km}^2$ , respectively.

493 During the 21 ka boreal winter, the Arctic Ocean and Baffin Bay are fully covered  
494 by ice and the ice around Greenland expands. The model displays increased sea ice in the  
495 western North Atlantic and decreased ice in the eastern North Atlantic and Nordic Seas  
496 where the prescribed FIS margin advances into the water (Fig. 2). The limit of substantial  
497 coverage north of  $55^\circ\text{N}$  is in agreement with reconstructions (de Vernal et al., 2006) and  
498 other LGM simulations (Otto-Bliesner et al., 2006a; Roche et al., 2007); however, slight  
499 fractional cover (pack ice) in the model likely extends too far south (to  $\sim 45^\circ\text{N}$ ) along the  
500 coast of North America. Fractional cover of up to 100% is simulated in the far Northwest  
501 Pacific and the Sea of Okhotsk with a sharp, southward transition to reduced coverage. In  
502 boreal summer of the LGM, simulated sea ice retreats to  $65^\circ\text{N}$  in the North Atlantic and  
503 persists along eastern Canada, Baffin Bay and south of Greenland and the extreme  
504 northern areas of the Nordic Seas.

505 The overall distribution of SH sea ice (Fig. 11) is in good agreement with  
506 reconstructions and other model simulations (Gersonde et al., 2005; Roche et al., 2012).  
507 The simulated LGM maximum winter sea ice area is  $35.5 \times 10^6 \text{ km}^2$  (72% greater than PI)  
508 and the LGM summer minimum is  $4.8 \times 10^6 \text{ km}^2$  (112% greater than PI); the winter and  
509 summer reconstructed areas are  $43.5 \pm 4 \times 10^6 \text{ km}^2$  and  $11.1 \pm 4 \times 10^6 \text{ km}^2$ , respectively  
510 (Roche et al., 2012). The seasonal amplitude (maximum minus minimum) of LGM ice  
511 cover simulated by GENMOM ( $30.6 \times 10^6 \text{ km}^2$ ) is comparable with the reconstructed  
512 amplitude ( $32.4 \pm 4 \times 10^6 \text{ km}^2$ ) and the LGM-to-PI change of seasonality is well within the  
513 range simulated by the PMIP2 models (Roche et al., 2012 their Figures 2 and 3).

514 **3.5 Antarctic Circumpolar Current and Atlantic Meridional Overturning**  
515 **Circulation**

516 The simulated ACC of 62 Sv is ~48% weaker than the observed value of 119 Sv  
517 through the Drake Passage (GECCO data; Köhl and Stammer, 2008). Although the T31  
518 resolution of GENMOM is a factor in limiting flow through the Drake Passage, we  
519 attribute the underestimate of the ACC in part to insufficient wind stress at the latitude of  
520 the Drake Passage, which is caused by equatorward displacement of the core of the  
521 westerly winds, a shortcoming in common with other low-resolution AOGCMs (Alder et  
522 al., 2011; Russell et al., 2006; Schmittner et al., 2011a).

523 Considerable uncertainty exists in the proxies that are used to infer past changes  
524 in AMOC strength (Delworth and Zeng, 2008; Lynch-Stieglitz et al., 2007). The  
525  $^{231}\text{Pa}/^{230}\text{Th}$  record from 33°N on the Bermuda Rise (Lippold et al., 2009; McManus et al.,  
526 2004) indicates that after the LGM the strength of the AMOC began to diminish at  
527 ~18 ka, was further reduced during Heinrich Event 1 (H1) at ~17 ka, increased abruptly  
528 during the BA at 15 ka, and weakened again during the YD cold reversal at ~12 ka. After  
529 the YD, the AMOC strengthened again and stabilized. In climate models, a variety of  
530 factors including the North Atlantic freshwater budget, model resolution and  
531 parameterizations and the characteristics of simulated Antarctic Bottom Water (AABW)  
532 give rise to a considerable simulated range of AMOC (Weber et al., 2007).

533 The AMOC in our PI simulation (Fig. 12) is  $19.3 \pm 1.4$  Sv at the core site of  
534 33°N, a value similar to the present-day estimate of  $18.7 \pm 4.8$  Sv at 26.5°N (Srokosz et  
535 al., 2012). The maximum AMOC simulated by GENMOM in the PI is 21.3 Sv at 41°N, a  
536 value outside the range of 13.8 to 20.8 Sv of five models in the PMIP2 experiments  
537 (Weber et al., 2007), but within the range of 3.8 to 31.7 Sv of the IPCC AR4

538 models (Meehl et al., 2007; Schmittner et al., 2005). The newer CMIP5 models have a  
539 narrower range of AMOC of ~14 to ~30 Sv when sampled at 30°N (Cheng et al., 2013);  
540 GENMOM simulates  $16.0 \pm 1.3$  Sv at this location.

541 Our simulated LGM AMOC at the core site is 16.4 Sv, which is a ~14.7%  
542 reduction relative to the PI. The maximum LGM AMOC is 22.4 Sv at 40.8°N, an  
543 increase of 1.1 Sv (5.1%) relative to the PI maximum and within the considerable range  
544 of -6.2 to +7.3 Sv in five PMIP2 simulations (Weber et al., 2007). In the deglacial  
545 simulations (21 ka through 15 ka), the northward (positive) AMOC flow extends deeper  
546 than that of the PI (Fig. 12) and the southward flow or AABW consequently is somewhat  
547 weakened. The maximum AMOC in GENMOM is essentially constant at 40.8°N depth  
548 of 1.23 km for all time slices. Although the depth of the maximum is again comparable to  
549 the range of the PMIP2 models ( $1.24 \pm 0.20$ ), the invariance of the location and depth in  
550 GENMOM is likely a model-specific response.

551 Our time slice simulations display an increase in the strength of AMOC from the  
552 LGM to a maximum at 15 ka, decrease to a minimum at 9 ka, and remain more-or-less  
553 constant through the PI (Fig. 13), which is in apparent disagreement with the  $^{231}\text{Pa}/^{230}\text{Th}$   
554 records from which greater variability is inferred (Lippold et al., 2009; McManus et al.,  
555 2004). We do not expect to capture rapid and abrupt climate change events such as H1  
556 (~17 ka), the BA (~15 ka) and the YD (~12 ka) with only eight time slices, because we  
557 did not manipulate freshwater discharge to the North Atlantic in our experimental design.

#### 558 **4 21 ka and 6 ka data-model comparisons**

559 We compare temperature and precipitation from our LGM and mid-Holocene  
560 simulations with paleoclimatic reconstructions and the PMIP3 simulations. For the LGM,

561 we use the pollen-based reconstructions of mean annual mean temperature (MAT) and  
562 precipitation (MAP) from Bartlein et al. (2011) over land, and the Multiproxy Approach  
563 for the Reconstruction of the Glacial Ocean Surface Project (MARGO) reconstructions  
564 over oceans (Waelbroeck et al., 2009). The gridded  $2^\circ \times 2^\circ$  pollen data include >3,000  
565 terrestrial pollen records from Eurasia, Africa and North America, and the global  
566 MARGO reconstruction comprises ~700 analyses of planktonic foraminifera, diatom,  
567 dinoflagellate cyst and radiolarian abundances, alkenones, and planktonic foraminifera  
568 Mg/Ca from marine core sites. For 6 ka, we combine the pollen-based reconstructions of  
569 Bartlein et al. (2011) and the GHOST SST reconstructions (Leduc et al., 2010). The 6 ka  
570 GHOST data set contains ~100 reconstructed temperature records based on analyses of  
571 alkenones and foraminifera Mg/Ca from marine sites located along continental margins  
572 and the Mediterranean Sea.

573 **4.1 21 ka**

574 Our simulated 21 ka anomalies of MAT and MAP are comparable with the pollen  
575 reconstructions (Fig. 14) and fall within the range of the PMIP3 models. GENMOM  
576 captures the mixed pattern of temperature and precipitation anomalies over Beringia that  
577 are present in the reconstructions (Fig. 14a,b) and in several of the PMIP3 simulations  
578 (SFigs. 8, 9, and 16). The GENMOM SST anomalies indicate broad cooling of the global  
579 oceans (mean of  $-1.7^\circ\text{C}$ ) but not as much cooling as is simulated in the PMIP3 models  
580 (mean of  $-2.9^\circ\text{C}$ ); although, Harrison et al. (2013) found that the PMIP3 models tended  
581 to overestimate oceanic cooling. Sampled at the MARGO locations, GENMOM is  
582 generally warmer, but within the range of the PMIP3 models (Harrison et al., 2013). The  
583 overall agreement of the simulation with the MARGO data is good, but some features in

584 the MARGO data are not reproduced by GENMOM. For example, similar to the PMIP3  
585 simulations (SFigs. 5, 6 and 16) the GENMOM simulation lacks the warming over the  
586 Greenland and Nordic Seas inferred from the data; although, while the data indicate the  
587 Nordic Sea was ice free at the LGM, the magnitude of the warming elsewhere, if it  
588 occurred, is somewhat unclear (de Vernal et al., 2006; Moller et al., 2013). The limited  
589 cooling along the western coast of North America and Mediterranean in GENMOM is  
590 attributed to the inability of the model to resolve the California Current and the  
591 Mediterranean circulation (Alder et al., 2011).

592 Over the tropical ocean basins, the 21 ka GENMOM simulation is 1.6 °C colder  
593 than the PI, in good agreement with the inferred MARGO cooling of  $1.7 \pm 1$  °C (Otto-  
594 Bliesner et al., 2009). Average simulated SST anomalies are also similar to MARGO  
595 over the Indian (-1.6 °C versus  $-1.4 \pm 0.7$  °C) and Pacific (-1.5 °C versus  $-1.2 \pm 1.1$  °C)  
596 Oceans, but are warmer than the data in the tropical Atlantic basin (-1.9 °C versus  $-2.9 \pm$   
597 1.3 °C). In each of these regions, the anomalies simulated by GENMOM fall within the  
598 range of six PMIP2 models analyzed by Otto-Bliesner et al. (2009). GENMOM captures  
599 the 2 – 4 °C cooling in the eastern coastal Atlantic evident in the MARGO data, and the  
600 SST anomalies are  $\sim 2 - 4$  °C colder over the Western Pacific Warm Pool. Neither  
601 GENMOM nor the PMIP3 simulations produce the warming over the central and eastern  
602 tropics, or the low latitudes and the North Atlantic that is evident in the MARGO  
603 reconstruction.

604 The simulated LGM MAP anomalies are also comparable with the pollen-based  
605 reconstructions (Fig. 14c and d). The model simulates general drying of the NH and a  
606 mix of increased and decreased precipitation in Beringia, South America, southern

607 Africa, Southeast (SE) Asia and Australia. GENMOM produces strong drying over and  
608 around the NH ice sheets, wetter-than-present conditions in the southwestern United  
609 States and drying in Central America. The simulation fails to reproduce the drying over  
610 eastern North America that is inferred from the pollen-based data. There is considerable  
611 variability in the PMIP3 simulations of MAP (SFigs. 9 and 10). In common with the  
612 PMIP3 models, GENMOM simulates a general reduction of precipitation over the NH,  
613 the North African and Indian monsoon regions, and SE Asia, and increased precipitation  
614 south of the LIS, southern Africa and much of Australia (SFig. 16).

615 **4.2 6 ka**

616 Relative to PI, the changes in 6 ka boundary conditions are predominantly in the  
617 seasonality of insolation (Table 1) as opposed to the stronger radiative forcing associated  
618 with changes in GHGs and continental ice sheets from the LGM through the early  
619 Holocene. The resulting changes in 6 ka climatology are thus more subtle than those of  
620 the deglaciation. The changes of 6 ka MAT simulated by GENMOM are generally within  
621 the range of  $\pm 1$  °C (Fig. 15b). Enhanced MAP and associated cooling are evident in the  
622 NH monsoonal regions (Fig. 15d). Elsewhere, MAP changes are within a range of  
623  $\pm 50$  mm.

624 Pollen-based data reconstructions indicate highly heterogeneous changes in MAT  
625 during 6 ka; however, there are regions with spatially consistent changes in sign, such as  
626 warming south of Hudson Bay, areas of warming over Scandinavia and Western Europe,  
627 and cooling in the Mediterranean region (Fig. 15a). Larger MAT changes at high-  
628 elevation sites and regions with anomalies of mixed sign occur in the data over most  
629 continents. The GENMOM 6 ka MAT anomalies also display a mix of warming and

630 cooling in a range of about  $\pm 4$  °C; however, where pollen-based records exist, the  
631 majority of the anomalies are within a narrower range of about  $\pm 1.5$  °C (Fig. 15b).  
632 GENMOM, and many of the PMIP3 models (SFigs. 8, 9 and 16), produce a mixture of  
633 warm and cold 6 ka MAT anomalies that are generally in the range of  $\pm 1$  °C over the  
634 North Atlantic, Europe and Scandinavia, which underestimates the proxy-based  
635 anomalies by  $>2$  °C at some sites.

636 The Asian pollen-based reconstruction similarly displays a heterogeneous  
637 temperature pattern that is reproduced by GENMOM and the PMIP3 models. In all of the  
638 models, the sign of the anomalies does not vary abruptly in close proximity to the pollen  
639 sites. We note, however, that the smooth topography in GCMs limits the ability of the  
640 models to reproduce large and regionally spatially heterogeneous anomalies that are  
641 characteristic of the local climate at many high elevation pollen sites in Western North  
642 America, the Alps, the central plateau of African and Asia.

643 GENMOM displays cooling in the North African and Indian monsoon regions  
644 and warming over the high northern latitudes, consistent with the PMIP3 models (Fig.  
645 15). In contrast, GENMOM simulates weak global cooling of 0.39 °C compared to no  
646 change in the PMIP3 model average which is partially attributed to our lower prescribed  
647 GHG concentrations (Table 1 caption).

648 Precipitation anomalies inferred from the pollen-based data indicate that 6 ka was  
649 wetter than the PI in Europe, Africa, Asia and some parts of western North America and  
650 drier than PI in much of eastern North America and Scandinavia (Fig. 15c). GENMOM  
651 simulates the gradients and coherent patterns of positive and negative MAP anomalies  
652 over North America, and North, Central and western Africa, in agreement with the data

653 and the PMIP3 models. The data and GENMOM are also in agreement over the Asian  
654 monsoon region and northwest Asia where wetter conditions prevail, but anomalies of  
655 opposite sign are simulated over the Great Lowland Plain in north central Eurasia and  
656 Southeast Asia. Bartlein et al. (2011) attribute cooling in Southeast Asia to a stronger  
657 winter monsoon at 6 ka. Our results (Figs. 6a and 8a), and many of the PMIP3 models,  
658 indicate cooler, drier winters (SFigs. 7 and 11) and regionally variable changes in the  
659 summer (SFigs. 8 and 12).

660 In Africa, the model captures the increase in precipitation in the northern and  
661 continental regions and drying along the southern coastal regions, as evident in the data.  
662 Strengthening of the African and Indian summer monsoons during the mid-Holocene  
663 corresponds well with the PMIP2 and PMIP3 models (Zheng and Braconnot, 2013). Both  
664 GENMOM and the data indicate drying over central Scandinavia, wetter conditions over  
665 east central Europe, the Iberian Peninsula and around the Mediterranean but, over  
666 Western Europe, the simulated decrease in MAP in GENMOM clearly disagrees with the  
667 data and some of the PMIP3 models (Figs. 15, SFigs. 7, 8 and 16); although, the  
668 magnitude of the change in the models is very small and the sign of the change varies  
669 among models. Wetter conditions also prevail in Indonesia, and a southwest-to-northeast  
670 wet-dry gradient is simulated over Australia.

## 671 **5 Summary**

672 We have presented a suite of multi-century equilibrium climate simulations with  
673 GENMOM for the past 21,000 years at 3,000-yr intervals. Each 1,100-yr simulation was  
674 forced with fixed, time-appropriate global boundary conditions that included insolation,  
675 GHGs, continental ice sheets and adjustment for sea level. The key drivers of climate

676 change from the LGM through the Holocene are retreat of the NH ice sheets, deglacial  
677 increased of GHG concentrations, and latitudinal and seasonal variations in insolation.

678 GENMOM reproduces reasonably well the LGM to Holocene temperature trends  
679 inferred from the paleoclimate data syntheses of Shakun et al. (2012) and Marcott et al.

680 (2013). The evolution of global temperature change simulated by GENMOM is  
681 consistent with three transient simulations, but is generally cooler during the deglacial  
682 time slices than the transient simulations when sampled at the proxy locations. The global  
683 LGM cooling of 3.8 °C simulated by GENMOM is within the range of 2.6 to 5.0 °C and  
684 average of 4.4 °C simulated by the PMIP3 models. Simulated LGM cooling of the  
685 tropical oceans is 1.6 °C, which is in good agreement with the MARGO reconstruction of  
686  $1.7 \pm 1$  °C. The weaker LGM global cooling is attributed to the sensitivity of GENMOM  
687 to CO<sub>2</sub> (2.2 °C for a 2X increase in the present-day value).

688 During the LGM, simulated precipitation is reduced globally by 8.2% and  
689 gradually increases through the Holocene to present-day values in response to loss of the  
690 NH ice sheets, global warming and related increases in atmospheric humidity. Between  
691 15 ka and 6 ka seasonal changes in insolation altered the NH land-sea temperature  
692 contrasts, which, combined with shifts in global circulation, strengthened the summer  
693 monsoons in Africa and India. Monsoonal precipitation in both regions peaked between  
694 12 ka and 9 ka, consistent with pollen-based reconstructions. The spatial patterns of mid-  
695 Holocene precipitation change simulated by GENMOM correspond well with the PMIP3  
696 models, as do the 6 ka changes in monsoonal precipitation. In contrast to the pollen-based  
697 reconstructions, GENMOM simulates slightly drier instead of slightly wetter-than-  
698 present in Western Europe.

699        The eight time slice simulations depict the glacial-interglacial transition that is in  
700    good agreement with other AOGCM simulations and compares reasonably well with  
701    data-based climate reconstructions. The data-model and model-model comparisons give  
702    us a measure of confidence that our paleo GENMOM simulations are reasonable on  
703    broad spatial scales and adds to the growing number of climate models that are capable of  
704    simulating key aspects of past climate change when constrained by a relatively small set  
705    of global boundary conditions. While our simulations are not continuous across the  
706    deglaciation and do not include events such as freshwater forcing, they do provide  
707    insights into between-period changes, such as altered NH storm tracks and strengthening  
708    of monsoons during the early to mid-Holocene and multi-century time series that are  
709    useful, for example, to explore ecosystem responses to changes in mean climate and the  
710    related interannual variability in the model. Future work using the model output produced  
711    by this study will address how internal model variability and multidecadal variability  
712    influence comparison with proxy data, particularly in North America using dynamical  
713    downscaling techniques.

Steve 1/28/15 11:48 AM

**Deleted:** The simulations provide insights into key dynamic features of the transition, such as altered NH storm tracks and strengthening of monsoons during the early to mid-Holocene.

714 **Appendix A: List of abbreviations and acronyms**

715	AABW	Antarctic Bottom Water
716	ACC	Antarctic Circumpolar Current
717	AMOC	Atlantic Meridional Overturning Circulation
718	AOGCM	Atmosphere-Ocean General Circulation Model
719	BA	Bølling-Allerød
720	CIS	Cordilleran Ice Sheet
721	CLIMAP	Climate: Long range Investigation, Mapping, and Prediction
722	COHMAP	Cooperative Holocene Mapping Project
723	DJF	December, January and February
724	FIS	Fennoscandian Ice Sheet
725	GECCO	German partner of Estimating the Circulation and Climate of the Ocean
726	GENESIS	Global Environmental and Ecological Simulation of Interactive Systems
727	GHG	Greenhouse gas
728	ITCZ	Intertropical Convergence Zone
729	H1	Heinrich Event 1
730	JJA	June, July and August
731	LGM	Last Glacial Maximum
732	LIS	Laurentide Ice Sheet
733	LSX	Land Surface eXchange
734	MAM	March, April and May
735	MAP	Mean annual precipitation
736	MARGO	Multiproxy Approach for the Reconstruction of the Glacial Ocean Surface Project
737	MAT	Mean annual temperature
739	MOM2	Modular Ocean Model version 2
740	NCAR	National Center for Atmospheric Research
741	NCEP	National Centers for Environmental Prediction
742	NH	Northern Hemisphere
743	OSU-LIS	Oregon State University Laurentide Ice Sheet
744	PD	Present-day
745	PI	Pre-industrial
746	PMIP	Palaeoclimate Modelling Intercomparison Project
747	SH	Southern Hemisphere
748	SLP	Sea-level pressure
749	SON	September, October and November
750	SST	Sea surface temperature
751	TEMPO	Testing Earth System Models with Paleoenvironmental Observations
752	YD	Younger Dryas
753		

753 **Acknowledgments**

754 We thank P. Bartlein, J. Shakun, S. Marcott, the MARGO and GHOST project  
755 members for providing their proxy reconstructions. Z. Liu and J. Zhu kindly provided  
756 time series data for the three transient models CCSM3, LOVECLIM and FAMOUS. We  
757 thank P. Bartlein, D. Pollard and R. Thompson for their thoughtful reviews and A.  
758 Schmittner, S. Marcott and P. Clark for helpful discussions and insights.

759

759 **References**

760 Alder, J. R., Hostetler, S. W., Pollard, D. and Schmittner, A.: Evaluation of a present-day  
 761 climate simulation with a new coupled atmosphere-ocean model GENMOM, *Geosci.  
 762 Model Dev.*, 4(1), 69–83, doi:10.5194/gmd-4-69-2011, 2011.

763 Annan, J. D. and Hargreaves, J. C.: A new global reconstruction of temperature changes  
 764 at the Last Glacial Maximum, *Clim Past*, 9(1), 367–376, doi:10.5194/cp-9-367-2013,  
 765 2013.

766 Bartlein, P. J., Harrison, S. P., Brewer, S., Connor, S., Davis, B. A. S., Gajewski, K.,  
 767 Guiot, J., Harrison-Prentice, T. I., Henderson, A., Peyron, O., Prentice, I. C., Scholze,  
 768 M., Seppä, H., Shuman, B., Sugita, S., Thompson, R. S., Viau, A. E., Williams, J. and  
 769 Wu, H.: Pollen-based continental climate reconstructions at 6 and 21 ka: a global  
 770 synthesis, *Clim Dynam*, 37(3-4), 775–802, doi:10.1007/s00382-010-0904-1, 2011.

771 Beckmann, B., Floegl, S., Hofmann, P., Schulz, M. and Wagner, T.: Orbital forcing of  
 772 Cretaceous river discharge in tropical Africa and ocean response, *Nature*, 437(7056),  
 773 241–244, doi:10.1038/nature03976, 2005.

774 Berger, A. and Loutre, M. F.: Insolation values for the climate of the last 10 million  
 775 years, *Quaternary Sci Rev*, 10(4), 297–317, doi:10.1016/0277-3791(91)90033-Q,  
 776 1991.

777 Bice, K. L., Birgel, D., Meyers, P. A., Dahl, K. A., Hinrichs, K.-U. and Norris, R. D.: A  
 778 multiple proxy and model study of Cretaceous upper ocean temperatures and  
 779 atmospheric CO<sub>2</sub> concentrations, *Paleoceanography*, 21(2), PA2002,  
 780 doi:10.1029/2005PA001203, 2006.

781 Braconnot, P., Harrison, S. P., Kageyama, M., Bartlein, P. J., Masson-Delmotte, V., Abe-  
 782 Ouchi, A., Otto-Bliesner, B. L. and Zhao, Y.: Evaluation of climate models using  
 783 palaeoclimatic data, *Nat Geosci*, 2(6), 417–424, doi:10.1038/nclimate1456, 2012.

784 Braconnot, P., Otto-Bliesner, B. L., Harrison, S., Joussaume, S., Peterschmitt, J. Y., Abe-  
 785 Ouchi, A., Crucifix, M., Driesschaert, E., Fichefet, T., Hewitt, C. D., Kageyama, M.,  
 786 Kitoh, A., Lainé, A., Loutre, M. F., Marti, O., Merkel, U., Ramstein, G., Valdes, P.,  
 787 Weber, S. L., Yu, Y. and Zhao, Y.: Results of PMIP2 coupled simulations of the Mid-  
 788 Holocene and Last Glacial Maximum - Part 1: experiments and large-scale features,  
 789 *Clim Past*, 3(2), 261–277, 2007a.

790 Braconnot, P., Otto-Bliesner, B. L., Harrison, S., Joussaume, S., Peterschmitt, J. Y., Abe-  
 791 Ouchi, A., Crucifix, M., Driesschaert, E., Fichefet, T., Hewitt, C. D., Kageyama, M.,  
 792 Kitoh, A., Loutre, M. F., Marti, O., Merkel, U., Ramstein, G., Valdes, P., Weber, L.,  
 793 Yu, Y. and Zhao, Y.: Results of PMIP2 coupled simulations of the Mid-Holocene and  
 794 Last Glacial Maximum - Part 2: feedbacks with emphasis on the location of the ITCZ  
 795 and mid- and high latitudes heat budget, *Clim Past*, 3(2), 279–296, 2007b.

796 Broccoli, A. J., Dahl, K. A. and Stouffer, R. J.: Response of the ITCZ to Northern  
 797 Hemisphere cooling, *Geophys. Res. Lett.*, 33(1), L01702,  
 798 doi:10.1029/2005GL024546, 2006.

799 Brohan, P., Kennedy, J. J., Harris, I., Tett, S. F. B. and Jones, P. D.: Uncertainty  
 800 estimates in regional and global observed temperature changes: A new data set from  
 801 1850, *J.-Geophys.-Res.*, 111(D12), doi:10.1029/2005JD006548, 2006.

802 Brook, E. J., Harder, S., Severinghaus, J., Steig, E. J. and Sucher, C. M.: On the origin  
 803 and timing of rapid changes in atmospheric methane during the last glacial period,  
 804 *Global Biogeochem Cy*, 14(2), 559–572, 2000.

805 Cheng, H., Sinha, A., Wang, X., Cruz, F. W. and Edwards, R. L.: The Global  
 806 Paleomonsoon as seen through speleothem records from Asia and the Americas, *Clim  
 807 Dynam*, 39(5), 1045–1062, doi:10.1007/s00382-012-1363-7, 2012.

808 Cheng, W., Chiang, J. C. H. and Zhang, D.: Atlantic Meridional Overturning Circulation  
 809 (AMOC) in CMIP5 Models: RCP and Historical Simulations, *J Climate*, 26(18),  
 810 7187–7197, doi:10.1175/JCLI-D-12-00496.1, 2013.

811 Chiang, J. C. H.: The Tropics in Paleoclimate, *Annual Review of Earth and Planetary  
 812 Sciences*, 37, 263–297, doi:10.1146/annurev.earth.031208.100217, 2009.

813 Chiang, J. C. H. and Bitz, C. M.: Influence of high latitude ice cover on the marine  
 814 Intertropical Convergence Zone, *Clim Dynam*, 25(5), 477–496, doi:10.1007/s00382-  
 815 005-0040-5, 2005.

816 Clark, P. U., Shakun, J. D., Baker, P. A., Bartlein, P. J., Brewer, S., Brook, E., Carlson,  
 817 A. E., Cheng, H., Kaufman, D. S., Liu, Z. Y., Marchitto, T. M., Mix, A. C., Morrill,  
 818 C., Otto-Bliesner, B. L., Pahnke, K., Russell, J. M., Whitlock, C., Adkins, J. F., Blois,  
 819 J. L., Clark, J., Colman, S. M., Curry, W. B., Flower, B. P., He, F., Johnson, T. C.,  
 820 Lynch-Stieglitz, J., Markgraf, V., McManus, J., Mitrovica, J. X., Moreno, P. I. and  
 821 Williams, J. W.: Global climate evolution during the last deglaciation, *P Natl Acad  
 822 Sci USA*, 109(19), E1134–E1142, doi:10.1073/pnas.1116619109, 2012.

823 Claussen, M.: Late Quaternary vegetation-climate feedbacks, *Clim Past*, 5(2), 203–216,  
 824 doi:10.5194/cp-5-203-2009, 2009.

825 CLIMAP Project Members: Seasonal reconstructions of the earth's surface at the Last  
 826 Glacial Maximum, *Geological Society of America, Map and Chart Series(MC-36)*,  
 827 1981.

828 COHMAP Members: Climatic Changes of the Last 18,000 Years - Observations and  
 829 Model Simulations, *Science*, 241(4869), 1043–1052, 1988.

830 de Vernal, A., Rosell-Mele, A., Kucera, M., Hillaire-Marcel, C., Eynaud, F., Weinelt, M.,  
 831 Dokken, T. and Kageyama, M.: Comparing proxies for the reconstruction of LGM

832 sea-surface conditions in the northern North Atlantic, *Quaternary Sci Rev*, 25(21-22),  
 833 2820–2834, doi:10.1016/j.quascirev.2006.06.006, 2006.

834 DeConto, R. M., Pollard, D. and Harwood, D.: Sea ice feedback and Cenozoic evolution  
 835 of Antarctic climate and ice sheets, *Paleoceanography*, 22(3), PA3214,  
 836 doi:10.1029/2006PA001350, 2007.

837 DeConto, R. M., Pollard, D., Wilson, P. A., Palike, H., Lear, C. H. and Pagani, M.:  
 838 Thresholds for Cenozoic bipolar glaciation, *Nature*, 455(7213), 652–656,  
 839 doi:10.1038/nature07337, 2008.

840 Delworth, T. L. and Zeng, F.: Simulated impact of altered Southern Hemisphere winds on  
 841 the Atlantic Meridional Overturning Circulation, *Geophys. Res. Lett.*, 35(20),  
 842 L20708, doi:10.1029/2008gl035166, 2008.

843 DiNezio, P. N. and Tierney, J. E.: The effect of sea level on glacial Indo-Pacific climate,  
 844 *Nature Geoscience*, 6(6), 1–7, doi:10.1038/ngeo1823, 2013.

845 Dorman, J. L. and Sellers, P. J.: A Global Climatology of Albedo, Roughness Length and  
 846 Stomatal-Resistance for Atmospheric General-Circulation Models as Represented by  
 847 the Simple Biosphere Model (Sib), *J Appl Meteorol*, 28(9), 833–855,  
 848 doi:10.1175/1520-0450(1989)028<0833:Agcoar>2.0.Co;2, 1989.

849 Dyke, A. S. and Prest, V. K.: Late Wisconsinan and Holocene history of the Laurentide  
 850 ice sheet, *Géographie physique et Quaternaire*, 1987.

851 Felzer, B.: Climate impacts of an ice sheet in East Siberia during the Last Glacial  
 852 Maximum, *Quaternary Sci Rev*, 20(1-3), 437–447, doi:10.1016/S0277-  
 853 3791(00)00106-2, 2001.

854 Felzer, B., Oglesby, R. J., Webb, T. and Hyman, D. E.: Sensitivity of a general  
 855 circulation model to changes in northern hemisphere ice sheets, *J.-Geophys.-Res.*,  
 856 101(D14), 19077–19092, 1996.

857 Felzer, B., Webb, T. and Oglesby, R. J.: The impact of ice sheets, CO<sub>2</sub>, and orbital  
 858 insolation on late quaternary climates: Sensitivity experiments with a general  
 859 circulation model, *Quaternary Sci Rev*, 17(6-7), 507–534, doi:10.1016/S0277-  
 860 3791(98)00010-9, 1998.

861 Flato, G. M. and Hibler, W. D.: Modeling Pack Ice as a Cavitating Fluid, *J. Phys.*  
 862 *Oceanogr.*, 22(6), 626–651, 1992.

863 Gasse, F.: Hydrological changes in the African tropics since the Last Glacial Maximum,  
 864 *Quaternary Sci Rev*, 19(1-5), 189–211, doi:10.1016/S0277-3791(99)00061-X, 2000.

865 Gates, W. L. and Nelson, A. B.: A new (revised) tabulation of the Scripps topography on  
 866 a 1 degree global grid. Part 1: Terrain heights, *Tech. Rep. R-1276-1-ARPA*. 1975.

867 Gent, P. R. and Mcwilliams, J. C.: Isopycnal Mixing in Ocean Circulation Models, *J.  
868 Phys. Oceanogr.*, 20(1), 150–155, doi:10.1175/1520-  
869 0485(1990)020<0150:IMIOCM>2.0.CO;2, 1990.

870 Gersonne, R., Crosta, X., Abelmann, A. and Armand, L.: Sea-surface temperature and sea  
871 ice distribution of the Southern Ocean at the EPILOG Last Glacial Maximum—a  
872 circum-Antarctic view based on siliceous microfossil records, *Quaternary Sci Rev*,  
873 24(7-9), 869–896, doi:10.1016/j.quascirev.2004.07.015, 2005.

874 Harrison, S. P., Bartlein, P. J., Brewer, S., Prentice, I. C., Boyd, M., Hessler, I.,  
875 Holmgren, K., Izumi, K. and Willis, K.: Climate model benchmarking with glacial  
876 and mid-Holocene climates, *Clim Dynam*, 1–18, doi:10.1007/s00382-013-1922-6,  
877 2013.

878 Harvey, L. D. D.: Development of a Sea Ice Model for Use in Zonally Averaged Energy  
879 Balance Climate Models, *J Climate*, 1(12), 1221–1238, 1988.

880 Hassol, S. J.: Impacts of a Warming Arctic - Arctic Climate Impact Assessment, *Impacts  
881 of a Warming Arctic - Arctic Climate Impact Assessment*, by Arctic Climate Impact  
882 Assessment, pp. 144. ISBN 0521617782. Cambridge, UK: Cambridge University  
883 Press, December 2004., -1, 2004.

884 Hély, C., Braconnot, P., Watrin, J. and Zheng, W.: Climate and vegetation: Simulating  
885 the African humid period, *Comptes Rendus Geoscience*, 341(8-9), 671–688,  
886 doi:10.1016/j.crte.2009.07.002, 2009.

887 Horton, D. E., Poulsen, C. J. and Pollard, D.: Orbital and CO<sub>2</sub> forcing of late Paleozoic  
888 continental ice sheets, *Geophys. Res. Lett.*, 34(19), L19708,  
889 doi:10.1029/2007GL031188, 2007.

890 Hostetler, S. W., Clark, P. U., Bartlein, P. J., Mix, A. C. and Pisias, N. J.: Atmospheric  
891 transmission of North Atlantic Heinrich events, *J.-Geophys.-Res.*, 104(D4), 3947–  
892 3952, 1999.

893 Hostetler, S. W., Pisias, N. and Mix, A. C.: Sensitivity of Last Glacial Maximum climate  
894 to uncertainties in tropical and subtropical ocean temperatures, *Quaternary Sci Rev*,  
895 25(11-12), 1168–1185, doi:10.1016/j.quascirev.2005.12.010, 2006.

896 Jaccard, S. L., Haug, G. H., Sigman, D. M., Pedersen, T. F., Thierstein, H. R. and Rohl,  
897 U.: Glacial/interglacial changes in subarctic North Pacific stratification, *Science*,  
898 308(5724), 1003–1006, doi:10.1126/science.1108696, 2005.

899 Joussaume, S., Taylor, K. E., Braconnot, P., mitchell, J., Kutzbach, J. E., Harrison, S. P.,  
900 Prentice, I. C., Broccoli, A. J., Abe-Ouchi, A., Bartlein, P. J., Bonfils, C., Dong, B.,  
901 Guiot, J., Herterich, K., Hewitt, C. D., Jolly, D., Kim, J. W., Kislov, A., Kitoh, A.,  
902 Loutre, M. F., Masson, V., McAvaney, B., McFarlane, N., de Noblet, N., Peltier, W.  
903 R., Peterschmitt, J. Y., Pollard, D., Rind, D., Royer, J. F., Schlesinger, M. E., Syktus,  
904 J., Thompson, S. L., Valdes, P., Vettoretti, G., Webb, R. S. and Wyputta, U.:

905 Monsoon changes for 6000 years ago: Results of 18 simulations from the  
 906 Paleoclimate Modeling Intercomparison Project (PMIP), *Geophys. Res. Lett.*, 26(7),  
 907 859–862, 1999.

908 Kageyama, M., D'Andrea, F., Ramstein, G., Valdes, P. J. and Vautard, R.: Weather  
 909 regimes in past climate atmospheric general circulation model simulations, *Clim  
 910 Dynam.*, 15(10), 773–793, doi:10.1007/S003820050315, 1999.

911 Kageyama, M., Laîné, A., Abe-Ouchi, A., Braconnot, P., Cortijo, E., Crucifix, M., de  
 912 Vernal, A., Guiot, J., Hewitt, C. D. and Kitoh, A.: Last Glacial Maximum  
 913 temperatures over the North Atlantic, Europe and western Siberia: a comparison  
 914 between PMIP models, MARGO sea–surface temperatures and pollen-based  
 915 reconstructions, *Quaternary Sci Rev*, 25(17–18), 2082–2102,  
 916 doi:10.1016/j.quascirev.2006.02.010, 2006.

917 Kalnay, E., Kanamitsu, M., Kistler, R., Collins, W., Deaven, D., Gandin, L., Iredell, M.,  
 918 Saha, S., White, G., Woollen, J., Zhu, Y., Chelliah, M., Ebisuzaki, W., Higgins, W.,  
 919 Janowiak, J., Mo, K. C., Ropelewski, C., Wang, J., Leetmaa, A., Reynolds, R., Jenne,  
 920 R. and Joseph, D.: The NCEP/NCAR 40-year reanalysis project, *Bull. Amer. Meteor.  
 921 Soc.*, 77(3), 437–471, 1996.

922 Kiehl, J. T., Hack, J. J., Bonan, G. B., Boville, B. A., Williamson, D. L. and Rasch, P. J.:  
 923 The National Center for Atmospheric Research Community Climate Model: CCM3, *J  
 924 Climate*, 11(6), 1131–1149, 1998.

925 Kim, S.-J., Crowley, T. J., Erickson, D. J., Govindasamy, B., Duffy, P. B. and Lee, B. Y.:  
 926 High-resolution climate simulation of the last glacial maximum, *Clim Dynam.*, 31(1),  
 927 1–16, doi:10.1007/s00382-007-0332-z, 2007.

928 Köhl, A. and Stammer, D.: Decadal sea level changes in the 50-year GECCO ocean  
 929 synthesis, *J Climate*, 21(9), 1876–1890, doi:10.1175/2007JCLI2081.1, 2008.

930 Köhler, P., Bintanja, R., Fischer, H., Joos, F., Knutti, R., Lohmann, G. and Masson-  
 931 Delmotte, V.: What caused Earth's temperature variations during the last 800,000  
 932 years? Data-based evidence on radiative forcing and constraints on climate  
 933 sensitivity, *Quaternary Sci Rev*, 29(1–2), 129–145,  
 934 doi:10.1016/j.quascirev.2009.09.026, 2010.

935 Kump, L. R. and Pollard, D.: Amplification of cretaceous warmth by biological cloud  
 936 feedbacks, *Science*, 320(5873), 195–195, doi:10.1126/science.1153883, 2008.

937 Kutzbach, J. E. and Liu, Z.: Response of the African Monsoon to Orbital Forcing and  
 938 Ocean Feedbacks in the Middle Holocene, *Science*, 278(5337), 440–443,  
 939 doi:10.1126/science.278.5337.440, 1997.

940 Kutzbach, J. E. and Otto-Bliesner, B. L.: The Sensitivity of the African-Asian Monsoonal  
 941 Climate to Orbital Parameter Changes for 9000 Years Bp in a Low-Resolution

942        General-Circulation Model, *Journal of the Atmospheric Sciences*, 39(6), 1177–1188,  
 943        1982.

944        Kutzbach, J. E., Bartlein, P. J., FOLEY, J. A., Harrison, S. P., Hostetler, S. W., Liu, Z.,  
 945        Prentice, I. C. and WEBB, T. I.: Potential role of vegetation feedback in the climate  
 946        sensitivity of high-latitude regions : A case study at 6000 years B.P, *Global*  
 947        *Biogeochem Cy*, 10(4), 727–736, 1996a.

948        Kutzbach, J., Bonan, G., Foley, J. and Harrison, S. P.: Vegetation and soil feedbacks on  
 949        the response of the African monsoon to orbital forcing in the early to middle  
 950        Holocene, *Nature*, 384(6610), 623–626, doi:10.1038/384623a0, 1996b.

951        Kutzbach, J., Gallimore, R., Harrison, S., Behling, P., Selin, R. and Laarif, F.: Climate  
 952        and biome simulations for the past 21,000 years, *Quaternary Sci Rev*, 17(6-7), 473–  
 953        506, 1998.

954        Leduc, G., Schneider, R., Kim, J. H. and Lohmann, G.: Holocene and Eemian sea surface  
 955        temperature trends as revealed by alkenone and Mg/Ca paleothermometry,  
 956        *Quaternary Sci Rev*, 29(7-8), 989–1004, doi:10.1016/j.quascirev.2010.01.004, 2010.

957        Lee, J.-Y. and Wang, B.: Future change of global monsoon in the CMIP5, *Clim Dynam*,  
 958        42(1-2), 101–119, doi:10.1007/s00382-012-1564-0, 2014.

959        Li, C. and Battisti, D. S.: Reduced Atlantic Storminess during Last Glacial Maximum:  
 960        Evidence from a Coupled Climate Model, *J Climate*, 21(14), 3561–3579,  
 961        doi:10.1175/2007jcli2166.1, 2008.

962        Licciardi, J. M., Clark, P. U., Jenson, J. W. and Macayeal, D. R.: Deglaciation of a soft-  
 963        bedded Laurentide Ice Sheet, *Quaternary Sci Rev*, 17(4-5), 427–448,  
 964        doi:10.1016/S0277-3791(97)00044-9, 1998.

965        Lippold, J., Grützner, J., Winter, D., Lahaye, Y., Mangini, A. and Christl, M.: Does  
 966        sedimentary  $^{231}\text{Pa}/^{230}\text{Th}$  from the Bermuda Rise monitor past Atlantic Meridional  
 967        Overturning Circulation? *Geophys. Res. Lett.*, 36(12), L12601,  
 968        doi:10.1029/2009gl038068, 2009.

969        Liu, Z., Otto-Bliesner, B. L., He, F., Brady, E. C., Tomas, R., Clark, P. U., Carlson, A. E.,  
 970        Lynch-Stieglitz, J., Curry, W., Brook, E., Erickson, D., Jacob, R., Kutzbach, J. and  
 971        Cheng, J.: Transient Simulation of Last Deglaciation with a New Mechanism for  
 972        Bolling-Allerod Warming, *Science*, 325(5938), 310–314,  
 973        doi:10.1126/science.1171041, 2009.

974        Liu, Z., Zhu, J., Rosenthal, Y., Zhang, X., Otto-Bliesner, B. L., Timmermann, A., Smith,  
 975        R. S., Lohmann, G., Zheng, W. and Elison Timm, O.: The Holocene temperature  
 976        conundrum, *Proceedings of the National Academy of Sciences*,  
 977        doi:10.1073/pnas.1407229111, 2014.

978 Lynch-Stieglitz, J., Adkins, J. F., Curry, W. B., Dokken, T., Hall, I. R., Herguera, J. C.,  
 979 Hirschi, J. J., Ivanova, E. V., Kissel, C., Marchal, O., Marchitto, T. M., McCave, I.  
 980 N., McManus, J. F., Mulitza, S., Ninnemann, U., Peeters, F., Yu, E. F. and Zahn, R.:  
 981 Atlantic meridional overturning circulation during the Last Glacial Maximum,  
 982 *Science*, 316(5821), 66–69, doi:10.1126/science.1137127, 2007.

983 Marcott, S. A., Shakun, J. D., Clark, P. U. and Mix, A. C.: A Reconstruction of Regional  
 984 and Global Temperature for the Past 11,300 Years, *Science*, 339(6124), 1198–1201,  
 985 doi:10.1126/Science.1228026, 2013.

986 Marzin, C. and Braconnot, P.: Variations of Indian and African monsoons induced by  
 987 insolation changes at 6 and 9.5 kyr BP, *Clim Dynam*, 33(2-3), 215–231,  
 988 doi:10.1007/s00382-009-0538-3, 2009.

989 McManus, J. F., Francois, R., Gherardi, J. M., Keigwin, L. D. and Brown-Leger, S.:  
 990 Collapse and rapid resumption of Atlantic meridional circulation linked to deglacial  
 991 climate changes, *Nature*, 428(6985), 834–837, doi:10.1038/Nature02494, 2004.

992 Meehl, G. A., Stocker, T. F. and Collins, W. D.: Global climate projections, in *Climate  
 993 Change 2007: The Physical Science Basis. Contribution of Working Group I to the  
 994 Fourth Assessment Report of the Intergovernmental Panel on Climate Change*, edited  
 995 by S. Solomon, D. Qin, M. Manning, Z. Chen, M. Marquis, K. B. Averyt, M. Tignor,  
 996 and H. L. Miller, Cambridge University Press, Cambridge, United Kingdom and New  
 997 York, NY, USA. 2007.

998 Miller, G., Mangan, J., Pollard, D., Thompson, S. L., Felzer, B. and Magee, J.: Sensitivity  
 999 of the Australian Monsoon to insolation and vegetation: Implications for human  
 1000 impact on continental moisture balance, *Geology*, 33(1), 65–68, 2005.

1001 Moller, T., Schulz, H. and Kucera, M.: The effect of sea surface properties on shell  
 1002 morphology and size of the planktonic foraminifer *Neogloboquadrina pachyderma* in  
 1003 the North Atlantic, *Palaeogeography, Palaeoclimatology, Palaeoecology*, 391, 34–48,  
 1004 doi:10.1016/j.palaeo.2011.08.014, 2013.

1005 Monnin, E., Indermuhle, A., Dallenbach, A., Fluckiger, J., Stauffer, B., Stocker, T. F.,  
 1006 Raynaud, D. and Barnola, J. M.: Atmospheric CO<sub>2</sub> concentrations over the last  
 1007 glacial termination, *Science*, 291(5501), 112–114, 2001.

1008 Otto-Bliesner, B. L., Brady, E. C., Clauzet, G., Tomas, R., Levis, S. and Kothavala, Z.:  
 1009 Last Glacial Maximum and Holocene climate in CCSM3, *J Climate*, 19(11), 2526–  
 1010 2544, doi:10.1175/Jcli3748.1, 2006a.

1011 Otto-Bliesner, B. L., Schneider, R., Brady, E. C., Kucera, M., Abe-Ouchi, A., Bard, E.,  
 1012 Braconnot, P., Crucifix, M., Hewitt, C. D., Kageyama, M., Marti, O., Paul, A.,  
 1013 Rosell-Mele, A., Waelbroeck, C., Weber, S. L., Weinelt, M. and Yu, Y.: A  
 1014 comparison of PMIP2 model simulations and the MARGO proxy reconstruction for  
 1015 tropical sea surface temperatures at last glacial maximum, *Clim Dynam*, 32(6), 799–  
 1016 815, doi:10.1007/s00382-008-0509-0, 2009.

1017 Otto-Bliesner, B. L., Tomas, R., Brady, E. C., Ammann, C., Kothaval, Z. and Clauzet,  
 1018 G.: Climate sensitivity of moderate- and low-resolution versions of CCSM3 to  
 1019 preindustrial forcings, *J Climate*, 19(11), 2567–2583, doi:10.1175/Jcli3754.1, 2006b.

1020 Pacanowski, R. C.: MOM 2 Version 2.0 (Beta) Documentation: User's Guide and  
 1021 Reference Manual, NOAA GFDL Ocean Technical Report 3.2. 1996.

1022 Pausata, F. S. R., Li, C., Wettstein, J. J., Kageyama, M. and Nisancioglu, K. H.: The key  
 1023 role of topography in altering North Atlantic atmospheric circulation during the last  
 1024 glacial period, *Clim Past*, 7(4), 1089–1101, doi:10.5194/cp-7-1089-2011, 2011.

1025 Peixoto, J. P. and Oort, A. H.: Physics of climate, American Institute of Physics, New  
 1026 York. 1992.

1027 Peltier, W. R.: Global glacial isostatic adjustment: palaeogeodetic and space-geodetic  
 1028 tests of the ICE-4G (VM2) model, *Journal of Quaternary Science*, 17(5-6), 491–510,  
 1029 doi:10.1002/jqs.713, 2002.

1030 Pinot, S., Ramstein, G., Harrison, S. P., Prentice, I. C., Guiot, J., Stute, M. and  
 1031 Joussaume, S.: Tropical paleoclimates at the Last Glacial Maximum: comparison of  
 1032 Paleoclimate Modeling Intercomparison Project (PMIP) simulations and paleodata,  
 1033 *Clim Dynam*, 15(11), 857–874, 1999.

1034 Pollard, D. and Reusch, D. B.: A calendar conversion method for monthly mean  
 1035 paleoclimate model output with orbital forcing, *J.-Geophys.-Res.*, 107(D22), 4615,  
 1036 doi:10.1029/2002JD002126, 2002.

1037 Pollard, D. and Thompson, S. L.: Sea-ice dynamics and CO<sub>2</sub>sensitivity in a global  
 1038 climate model, *Atmosphere-Ocean*, 32(2), 449–467,  
 1039 doi:10.1080/07055900.1994.9649506, 1994.

1040 Pollard, D. and Thompson, S. L.: Use of a Land-Surface-Transfer Scheme (Lsx) in a  
 1041 Global Climate Model - the Response to Doubling Stomatal-Resistance, *Global  
 1042 Planet Change*, 10(1-4), 129–161, doi:10.1016/0921-8181(94)00023-7, 1995.

1043 Pollard, D. and Thompson, S. L.: Climate and ice-sheet mass balance at the last glacial  
 1044 maximum from the genesis version 2 global climate model, *Quaternary Sci Rev*,  
 1045 16(8), 841–863, 1997.

1046 Pollard, D., Bergengren, J. C., Stillwell-Soller, L. M., Felzer, B. and Thompson, S. L.:  
 1047 Climate simulations for 10000 and 6000 years BP using the GENESIS global climate  
 1048 model. *Palaeoclimates: Data and Modelling, Palaeoclimates - Data and Modelling*,  
 1049 1998.

1050 Poulsen, C. J., Pollard, D. and White, T. S.: General circulation model simulation of the  
 1051 delta O-18 content of continental precipitation in the middle Cretaceous: A model-  
 1052 proxy comparison, *Geology*, 35(3), 199–202, doi:10.1130/G23343A.1, 2007a.

1053 Poulsen, C. J., Pollard, D., Montanez, I. P. and Rowley, D.: Late Paleozoic tropical  
 1054 climate response to Gondwanan deglaciation, *Geology*, 35(9), 771–774,  
 1055 doi:10.1130/G23841A.1, 2007b.

1056 Ramstein, G. and Joussaume, S.: Sensitivity experiments to sea surface temperatures, sea-  
 1057 ice extent and ice-sheet reconstruction for the Last Glacial Maximum, *Annals of*  
 1058 *Glaciology*, 21, 343–347, 1995.

1059 Renssen, H., Goosse, H., Fichefet, T., Brovkin, V., Driesschaert, E. and Wolk, F.:  
 1060 Simulating the Holocene climate evolution at northern high latitudes using a coupled  
 1061 atmosphere-sea ice-ocean-vegetation model, *Clim Dynam*, 24(1), 23–43,  
 1062 doi:10.1007/s00382-004-0485-y, 2004.

1063 Rind, D.: Components of the Ice-Age Circulation, *J.-Geophys.-Res.*, 92(D4), 4241–4281,  
 1064 1987.

1065 Roche, D. M., Crosta, X. and Renssen, H.: Evaluating Southern Ocean sea-ice for the  
 1066 Last Glacial Maximum and pre-industrial climates: PMIP-2 models and data  
 1067 evidence, *Quaternary Sci Rev*, 56, 99–106, doi:10.1016/j.quascirev.2012.09.020,  
 1068 2012.

1069 Roche, D. M., Dokken, T. M., Goosse, H., Renssen, H. and Weber, S. L.: Climate of the  
 1070 Last Glacial Maximum: sensitivity studies and model-data comparison with the  
 1071 LOVECLIM coupled model, *Clim Past*, 3(2), 205–224, 2007.

1072 Rohling, E. J., Medina-Elizalde, M., Shepherd, J. G., Siddall, M. and Stanford, J. D.: Sea  
 1073 Surface and High-Latitude Temperature Sensitivity to Radiative Forcing of Climate  
 1074 over Several Glacial Cycles, *J. Climate*, 25(5), 1635–1656,  
 1075 doi:10.1175/2011JCLI4078.1, 2012.

1076 Ruddiman, W. F., Vavrus, S. J. and Kutzbach, J. E.: A test of the overdue-glaciation  
 1077 hypothesis, *Quaternary Sci Rev*, 24(1-2), 1–10, doi:10.1016/j.quascirev.2004.07.010,  
 1078 2005.

1079 Russell, J. L., Stouffer, R. J. and Dixon, K. W.: Intercomparison of the Southern Ocean  
 1080 circulations in IPCC coupled model control simulations, *J Climate*, 19(18), 4560–  
 1081 4575, doi:10.1175/Jcli3869.1, 2006.

1082 Schmittner, A., Latif, M. and Schneider, B.: Model projections of the North Atlantic  
 1083 thermohaline circulation for the 21st century assessed by observations, *Geophys. Res.*  
 1084 *Lett.*, 32(23), L23710, doi:10.1029/2005gl024368, 2005.

1085 Schmittner, A., Silva, T. A. M., Fraedrich, K., Kirk, E. and Lunkeit, F.: Effects of  
 1086 Mountains and Ice Sheets on Global Ocean Circulation, *J Climate*, 24(11), 2814–  
 1087 2829, doi:10.1175/2010jcli3982.1, 2011a.

1088 Schmittner, A., Urban, N. M., Shakun, J. D., Mahowald, N. M., Clark, P. U., Bartlein, P.  
 1089 J., Mix, A. C. and Rosell-Mele, A.: Climate sensitivity estimated from temperature

1090 reconstructions of the Last Glacial Maximum, *Science*, 334(6061), 1385–1388,  
 1091 doi:10.1126/science.1203513, 2011b.

1092 Semtner, A. J.: A Model for the Thermodynamic Growth of Sea Ice in Numerical  
 1093 Investigations of Climate, *J. Phys. Oceanogr.*, 6(3), 379–389, doi:10.1175/1520-  
 1094 0485(1976)006<0379:AMFTTG>2.0.CO;2, 1976.

1095 Shakun, J. D., Clark, P. U., He, F., Marcott, S. A., Mix, A. C., Liu, Z., Otto-Bliesner, B.  
 1096 L., Schmittner, A. and Bard, E.: Global warming preceded by increasing carbon  
 1097 dioxide concentrations during the last deglaciation, *Nature*, 484(7392), 49–54,  
 1098 doi:10.1038/nature10915, 2012.

1099 Singarayer, J. S. and Valdes, P. J.: High-latitude climate sensitivity to ice-sheet forcing  
 1100 over the last 120 kyr, *Quaternary Sci Rev*, 29(1-2), 43–55,  
 1101 doi:10.1016/j.quascirev.2009.10.011, 2010.

1102 Smith, R. S. and Gregory, J.: The last glacial cycle: transient simulations with an  
 1103 AOGCM, *Clim Dynam*, 38(7-8), 1545–1559, doi:10.1007/s00382-011-1283-y, 2012.

1104 Sowers, T., Alley, R. B. and Jubenville, J.: Ice core records of atmospheric N<sub>2</sub>O covering  
 1105 the last 106,000 years, *Science*, 301(5635), 945–948, 2003.

1106 Srokosz, M., Baringer, M., Bryden, H., Cunningham, S., Delworth, T., Lozier, S.,  
 1107 Marotzke, J. and Sutton, R.: Past, Present, and Future Changes in the Atlantic  
 1108 Meridional Overturning Circulation, *Bull. Amer. Meteor. Soc.*, 93(11), 1663–1676,  
 1109 doi:10.1175/bams-d-11-00151.1, 2012.

1110 Tabor, C. R., Poulsen, C. J. and Pollard, D.: Mending Milankovitch's theory: obliquity  
 1111 amplification by surface feedbacks, *Clim Past*, 10(1), 41–50, doi:10.5194/cp-10-41-  
 1112 2014, 2014.

1113 Thompson, S. L. and Pollard, D.: A Global Climate Model (Genesis) with a Land-Surface  
 1114 Transfer Scheme (Lsx) .1. Present Climate Simulation, *J Climate*, 8(4), 732–761,  
 1115 1995.

1116 Thompson, S. L. and Pollard, D.: Greenland and Antarctic mass balances for present and  
 1117 doubled atmospheric CO<sub>2</sub> from the GENESIS version-2 global climate model, *J  
 1118 Climate*, 10(5), 871–900, 1997.

1119 Timm, O. and Timmermann, A.: Simulation of the Last 21 000 Years Using Accelerated  
 1120 Transient Boundary Conditions, *J Climate*, 20(17), 4377–4401,  
 1121 doi:10.1175/JCLI4237.1, 2007.

1122 Timm, O., Köhler, P., Timmermann, A. and Menzel, L.: Mechanisms for the onset of the  
 1123 African humid period and Sahara greening 14.5–11 ka BP, *J Climate*, 23(10), 2612–  
 1124 2633, doi:10.1175/2010jcli3217.1, 2010.

1125 Timm, O., Timmermann, A., Abe-Ouchi, A., Saito, F. and Segawa, T.: On the definition  
 1126 of seasons in paleoclimate simulations with orbital forcing, *Paleoceanography*, 23(2),  
 1127 PA2221, doi:10.1029/2007PA001461, 2008.

1128 Ullman, D. J., LeGrande, A. N., Carlson, A. E., Anslow, F. S. and Licciardi, J. M.:  
 1129 Assessing the impact of Laurentide Ice Sheet topography on glacial climate, *Clim  
 1130 Past*, 10(2), 487–507, doi:10.5194/cp-10-487-2014, 2014.

1131 Unterman, M. B., Crowley, T. J., Hodges, K. I., Kim, S. J. and Erickson, D. J.:  
 1132 Paleometeorology: High resolution Northern Hemisphere wintertime mid-latitude  
 1133 dynamics during the Last Glacial Maximum, *Geophys. Res. Lett.*, 38(23), L23702,  
 1134 doi:10.1029/2011gl049599, 2011.

1135 Waelbroeck, C., Paul, A., Kucera, M., Rosell-Mele, A., Weinelt, M., Schneider, R., Mix,  
 1136 A. C., Abelmann, A., Armand, L., Bard, E., Barker, S., Barrows, T. T., Benway, H.,  
 1137 Cacho, I., Chen, M. T., Cortijo, E., Crosta, X., de Vernal, A., Dokken, T., Duprat, J.,  
 1138 Elderfield, H., Eynaud, F., Gersonde, R., Hayes, A., Henry, M., Hillaire-Marcel, C.,  
 1139 Huang, C. C., Jansen, E., Juggins, S., Kallel, N., Kiefer, T., Kienast, M., Labeyrie, L.,  
 1140 Leclaire, H., Londeix, L., Mangin, S., Matthiessen, J., Marret, F., Meland, M., Morey,  
 1141 A. E., Mulitza, S., Pflaumann, U., Pisias, N. G., Radi, T., Rochon, A., Rohling, E. J.,  
 1142 Sbaffi, L., Schaefer-Neth, C., Solignac, S., Spero, H., Tachikawa, K., Turon, J. L. and  
 1143 Members, M. P.: Constraints on the magnitude and patterns of ocean cooling at the  
 1144 Last Glacial Maximum, *Nature Geoscience*, 2(2), 127–132, doi:10.1038/Ngeo411,  
 1145 2009.

1146 Weber, S. L., Drijfhout, S. S., Abe-Ouchi, A., Crucifix, M., Eby, M., Ganopolski, A.,  
 1147 Murakami, S., Otto-Bliesner, B. L. and Peltier, W. R.: The modern and glacial  
 1148 overturning circulation in the Atlantic Ocean in PMIP coupled model simulations,  
 1149 *Clim Past*, 3(1), 51–64, 2007.

1150 Zhao, Y. and Harrison, S. P.: Mid-Holocene monsoons: a multi-model analysis of the  
 1151 inter-hemispheric differences in the responses to orbital forcing and ocean feedbacks,  
 1152 *Clim Dynam*, 39(6), 1457–1487, doi:10.1007/s00382-011-1193-z, 2012.

1153 Zheng, W. and Braconnot, P.: Characterization of Model Spread in PMIP2 Mid-Holocene  
 1154 Simulations of the African Monsoon, *J Climate*, 26(4), 1192–1210,  
 1155 doi:10.1175/JCLI-D-12-00071.1, 2013.

1156 Zhou, J., Poulsen, C. J., Pollard, D. and White, T. S.: Simulation of modern and middle  
 1157 Cretaceous marine  $\delta^{18}\text{O}$  with an ocean-atmosphere general circulation model,  
 1158 *Paleoceanography*, 23(3), PA3223, doi:10.1029/2008pa001596, 2008.

1159

1160

1160

1161 Table 1. Atmospheric greenhouse gas concentrations for each time slice simulation. The  
 1162 21 ka through 3 ka values for CO<sub>2</sub> (Monnin et al., 2001), CH<sub>4</sub> (Brook et al., 2000) and  
 1163 N<sub>2</sub>O (Sowers et al., 2003) are estimated from ice core records by averaging the gas  
 1164 concentrations within a  $\pm 300$  yr window centered at the time of interest. For comparison,  
 1165 the PMIP3 concentrations for 6 ka are 280 ppmV, 650 ppbV, and 270 ppbV for CO<sub>2</sub>, CH<sub>4</sub>  
 1166 and N<sub>2</sub>O respectively, and 185 ppmV, 350 ppbV, and 200 ppbV for 21 ka. In the table,  $e$   
 1167 is eccentricity,  $\omega-180$  is precession and  $\varepsilon$  is obliquity (Berger and Loutre, 1991).

	CO <sub>2</sub> (ppmV)	CH <sub>4</sub> (ppbV)	N <sub>2</sub> O (ppbV)	$e$	$\omega-180$	$\varepsilon$
PD	355	1714	311	0.0176	101.37	23.446
PI	280	760	270	0.0176	101.37	23.446
3 ka	275	627	264	0.0183	50.30	23.815
6 ka	260	596	227	0.0192	0.01	24.100
9 ka	260	677	244	0.0198	310.32	24.229
12 ka	240	500	246	0.0201	261.07	24.161
15 ka	220	500	216	0.0202	212.04	23.895
18 ka	188	382	219	0.0199	163.04	23.475
21 ka	188	392	199	0.0194	113.98	22.989

1168

1169

1170

1170 Table 2. Annual average 2-m air temperatures and precipitation rates for the time slice  
 1171 simulations. NCEP is from the National Center for Environmental Prediction  
 1172 NCEP/NCAR Reanalysis data set (Kalnay et al., 1996), PD2X is the 2xCO<sub>2</sub> simulation,  
 1173 PD is present day and PI is pre-industrial. Parenthetical values are the changes from the  
 1174 previous time slice, e.g., the global average temperature for the PD is 0.77 °C warmer  
 1175 than the PI.

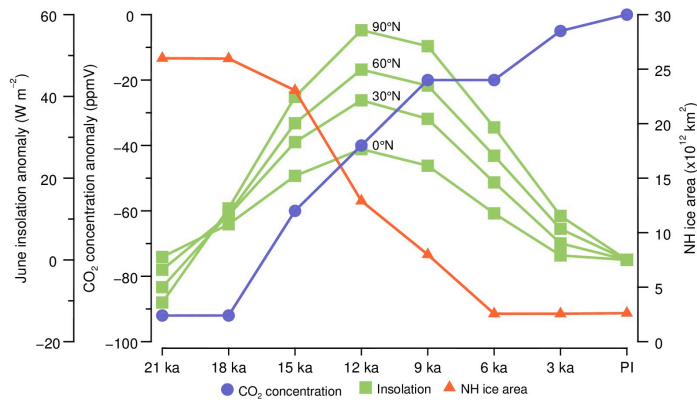
	Temperature (K)			Precipitation (mm d <sup>-1</sup> )		
	Global	Land	Ocean	Global	Land	Ocean
NCEP (1980-2000)	287.52 --	281.66 --	289.84 --	3.09 --	2.30 --	3.40 --
PD2X	288.48 (2.2)	282.06 (2.69)	291.29 (1.91)	3.11 (0.11)	2.17 (0.10)	3.53 (0.13)
PD	286.34 (0.77)	279.37 (0.93)	289.38 (0.70)	3.00 (0.04)	2.07 (0.04)	3.40 (0.05)
PI	285.57 (0.07)	278.44 (-0.03)	288.68 (0.15)	2.95 (0.00)	2.03 (-0.02)	3.36 (0.02)
3 ka	285.50 (0.32)	278.47 (0.30)	288.53 (0.33)	2.95 (0.02)	2.05 (0.00)	3.34 (0.04)
6 ka	285.17 (0.23)	278.18 (0.95)	288.20 (-0.27)	2.93 (0.02)	2.05 (0.00)	3.30 (0.02)
9 ka	284.95 (0.74)	277.23 (1.63)	288.47 (0.22)	2.91 (0.05)	2.05 (0.06)	3.30 (0.03)
12 ka	284.21 (1.40)	275.60 (2.44)	288.25 (0.70)	2.86 (0.09)	1.99 (0.12)	3.26 (0.05)
15 ka	282.81 (0.93)	273.16 (1.53)	287.55 (0.53)	2.77 (0.05)	1.87 (0.09)	3.21 (0.02)
18 ka	281.88 (0.16)	271.63 (0.28)	287.02 (0.06)	2.72 (0.01)	1.78 (0.01)	3.19 (0.01)
21 ka	281.72	271.35	286.96	2.71	1.78	3.18

1176

1177

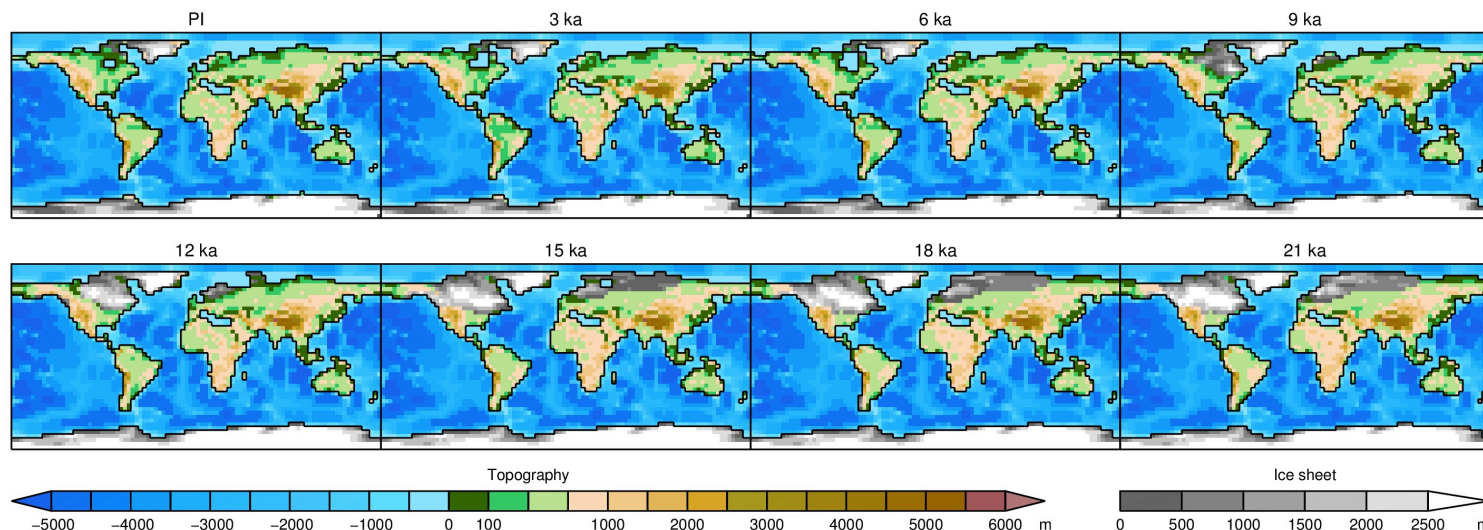
1178

1179



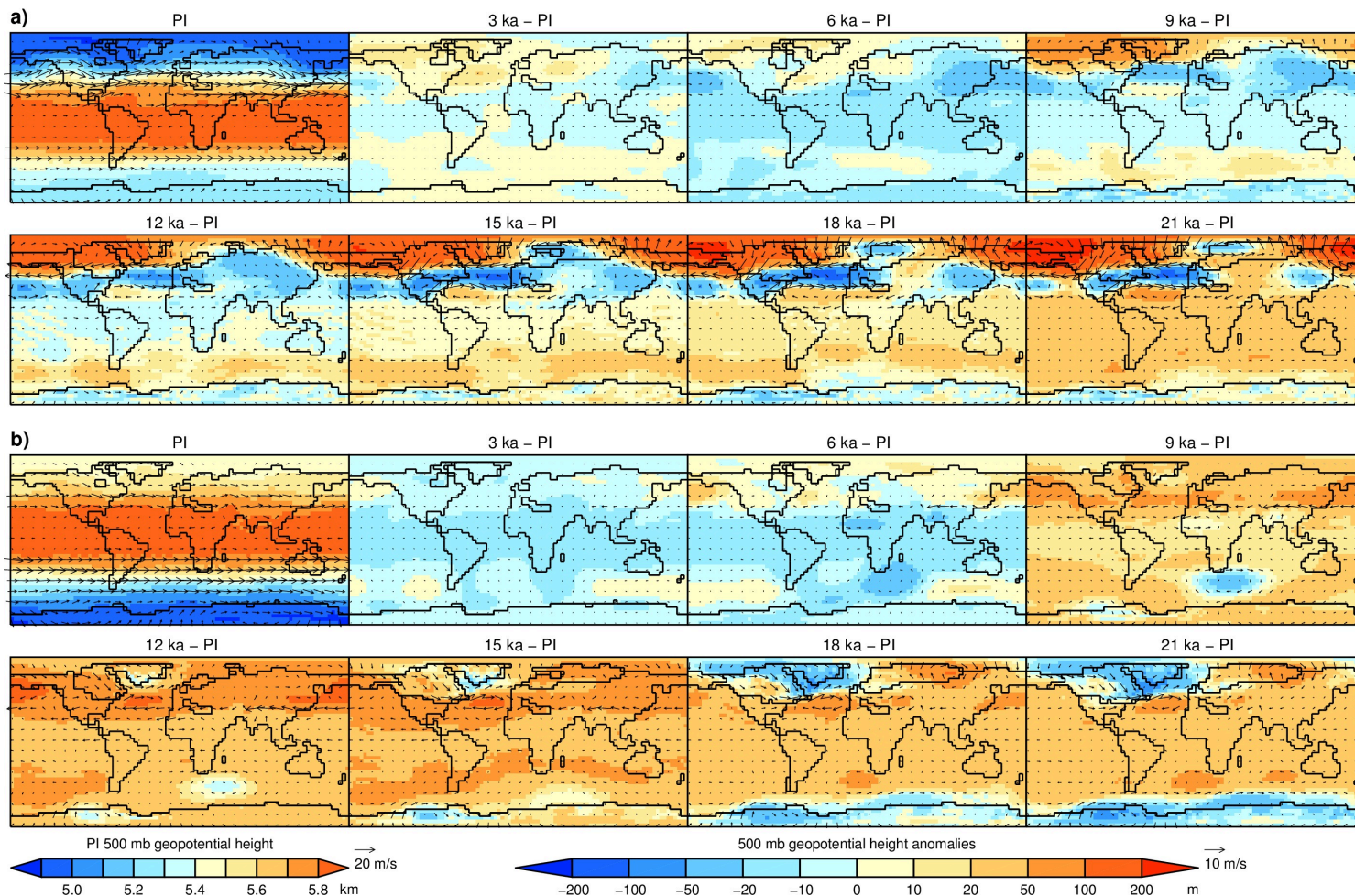
1180

1181 Fig. 1. Boundary conditions for the time slice simulations. CO<sub>2</sub> concentrations are  
 1182 relative to the PI concentration of 280 ppmV. NH ice area is the total area covered by the  
 1183 continental ice sheets. June insolation anomalies are relative to PI at the indicated  
 1184 latitudes. Mid-month insolation data from Berger and Loutre (1991).



1185  
1186

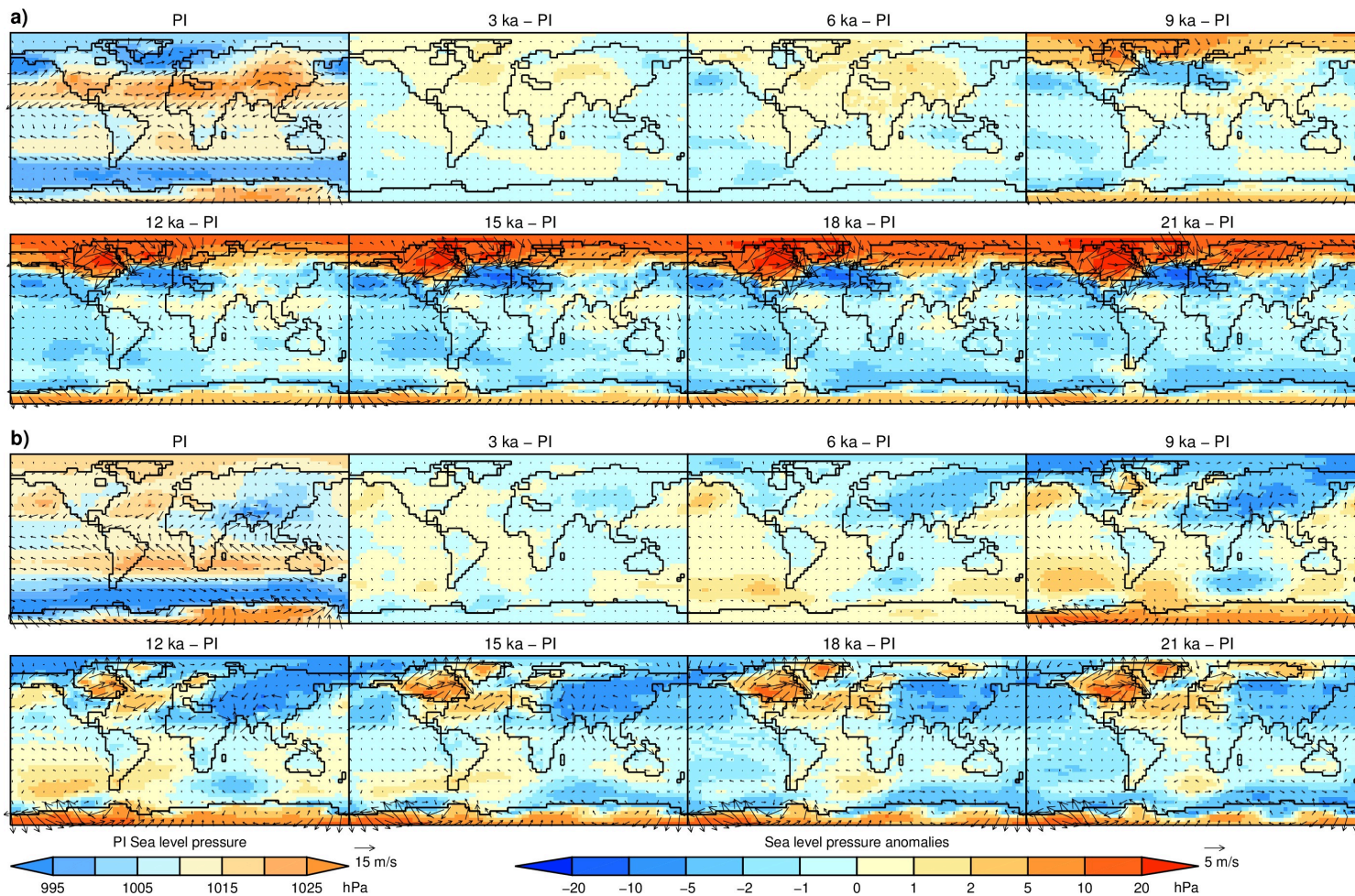
Fig. 2. Orography for the time slice simulations, with ice sheet height and extent derived from ICE-4G (Peltier, 2002) for the  
1187 Fennoscandian, Cordilleran and Antarctic, and OSU-LIS (Licciardi et al., 1998) for the Laurentide.



1188

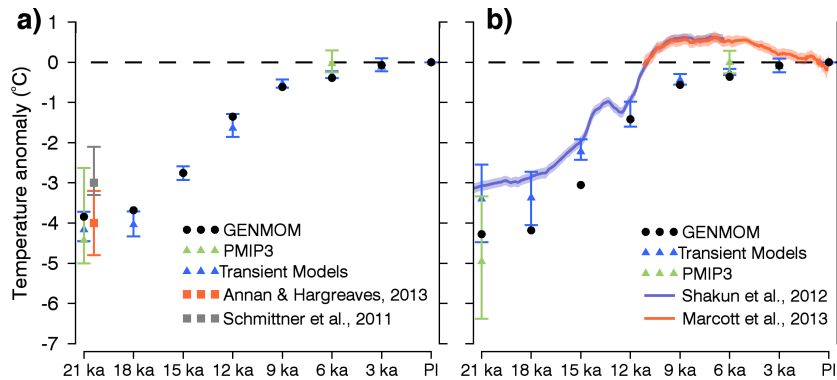
1189 Fig. 3. Simulated seasonal 500 hPa geopotential height and wind anomalies relative to PI. a) December, January, and February and b)

1190 June, July and August. Raw 500 hPa geopotential height and wind are shown in SFig. 2.



1191  
1192 Fig. 4. Simulated seasonal average sea-level pressure and 2-m wind anomalies relative to PI. a) December, January, and February and  
1193 b) June, July, and August. Raw sea level pressure and wind are shown in SFig. 3.

1194

1195  
1196

1197 Fig. 5. Simulated and reconstructed changes in temperature from 21 ka to present. a)

1198 Global mean surface air temperature from GENMOM compared to the PMIP3 ensemble

1199 average and three transient models (CCSM (Liu et al., 2009), LOVECLIM (Timm and

1200 Timmermann, 2007) and FAMOUS (Smith and Gregory, 2012)). The transient model

1201 values are averages over a  $\pm 50$  yr window centered on the eight time slices. The symbols

1202 for the PMIP and transient models are the average of the ensembles and the bars

1203 represent the range of the ensembles. Data-model estimates of mean and range of LGM

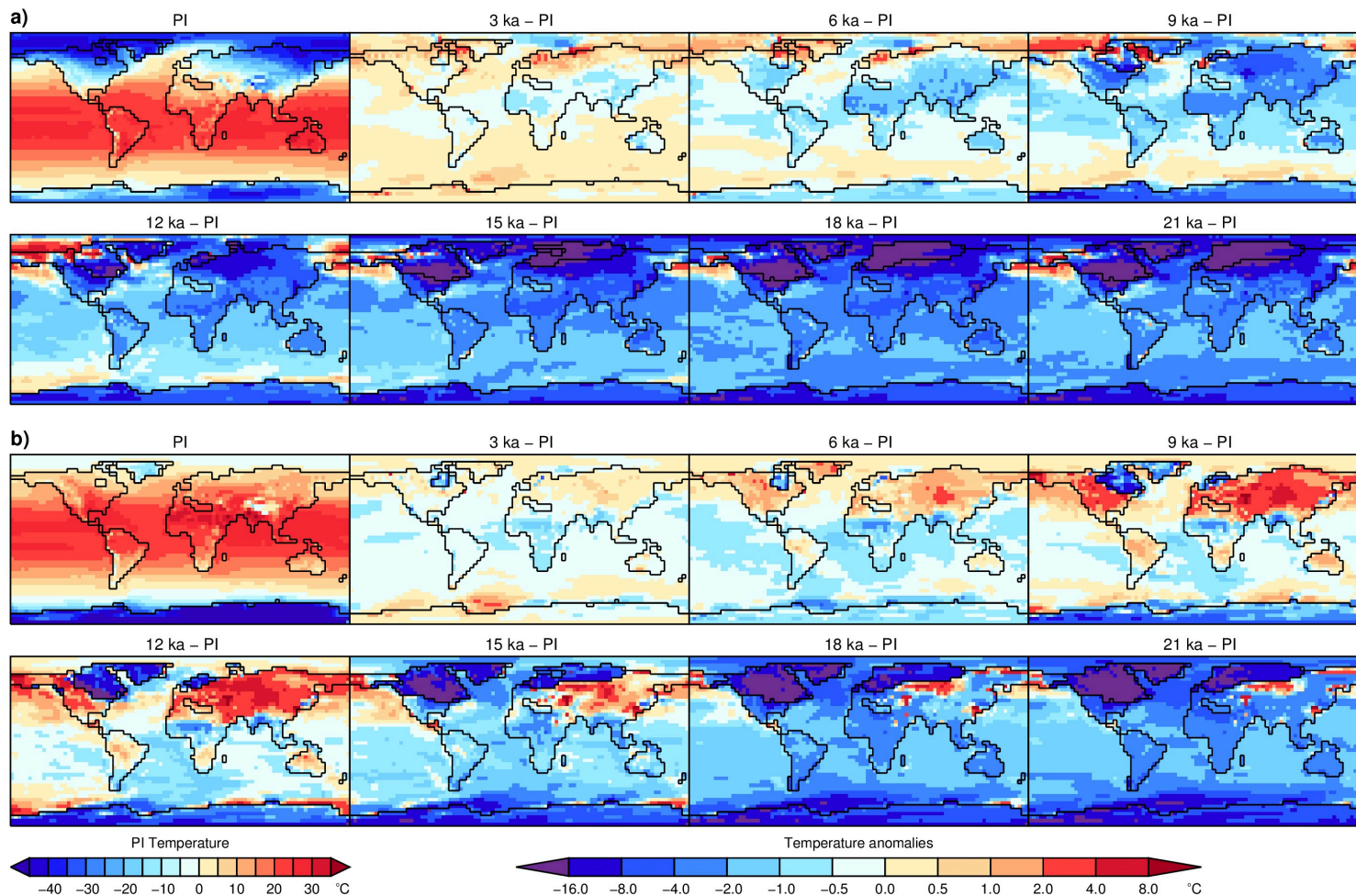
1204 cooling by Annan and Hargreaves (2013) and Schmittner et al. (2011b) are offset from

1205 21 ka for legibility. b) Temperature change at the proxy sites used in the reconstructions

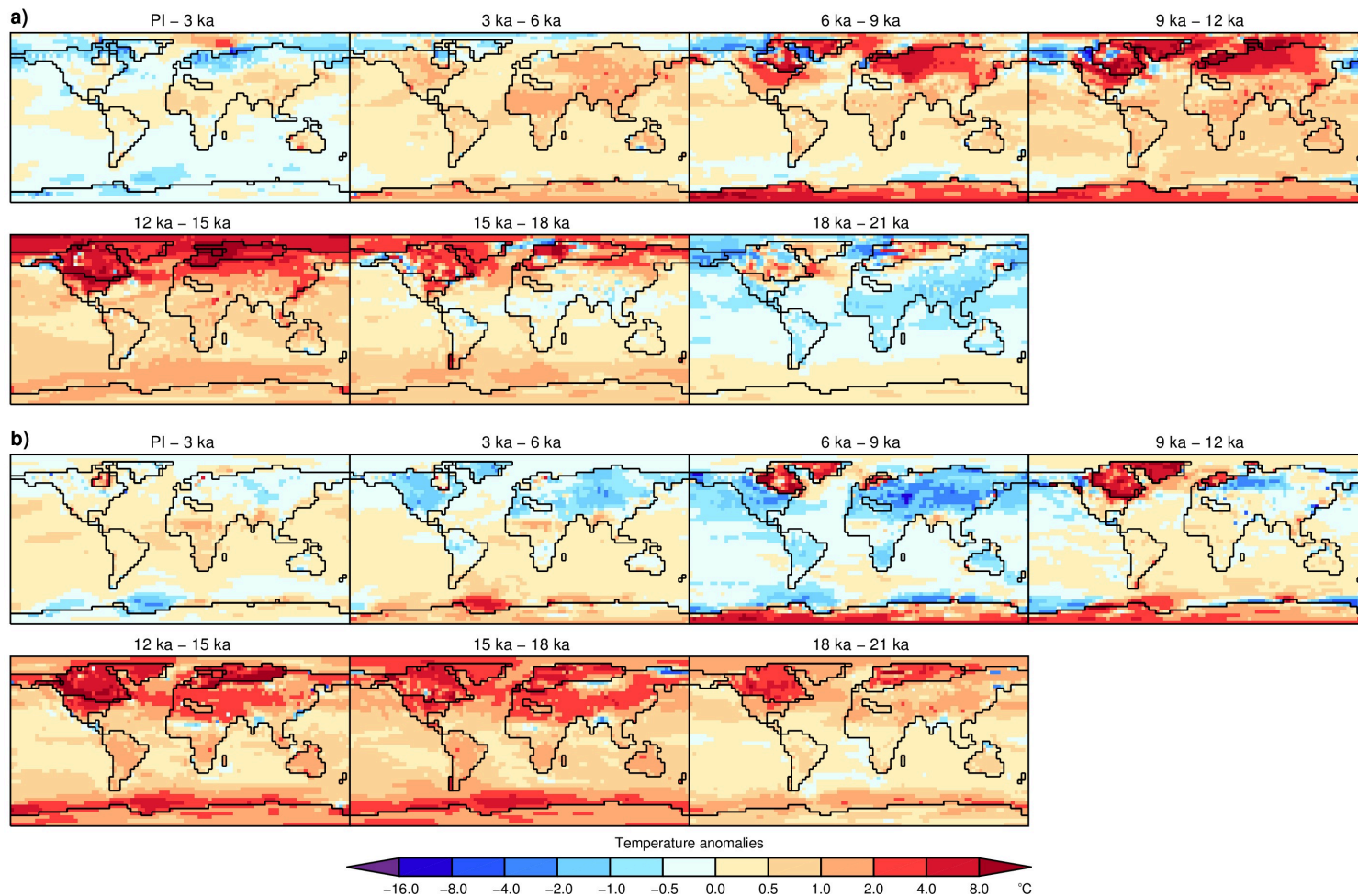
1206 by Shakun et al. (2012) and Marcott et al (2013). The models were bilinearly interpolated

1207 and aggregated to the  $5^\circ \times 5^\circ$  boxes around the proxy sites as in Marcott et al. (2013).

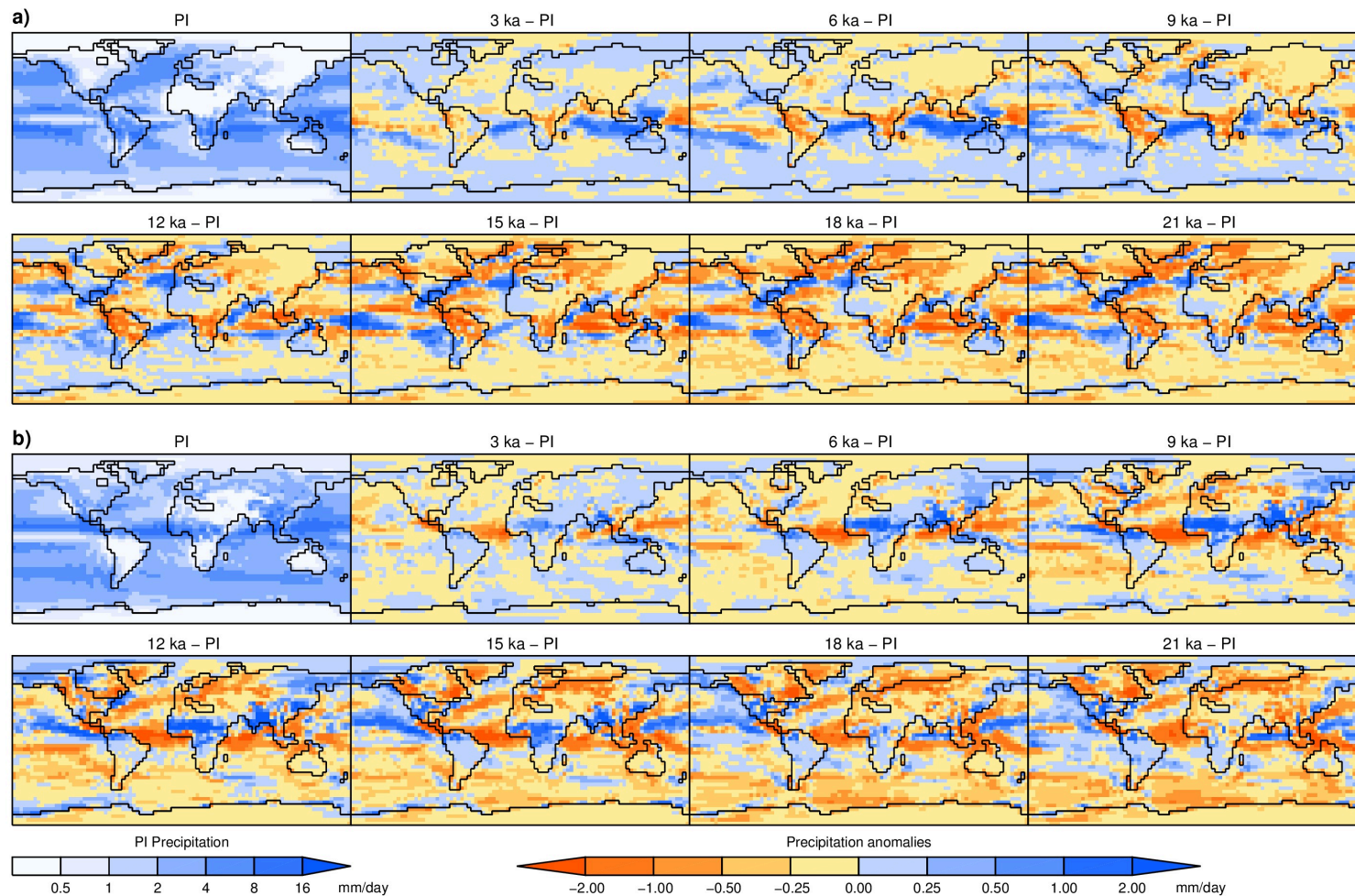
1208 The  $1\sigma$  uncertainty in the reconstructions is indicated by the shaded band. Marcott et al.  
1209 (2013) is adjusted to a pre-industrial (~1850) base value rather than the original 1961-  
1210 1990. Data younger than pre-industrial are removed. The Shakun et al. (2012) and  
1211 Marcott et al. (2013) time series are joined at their 11.5 ka – 6.5 ka means.



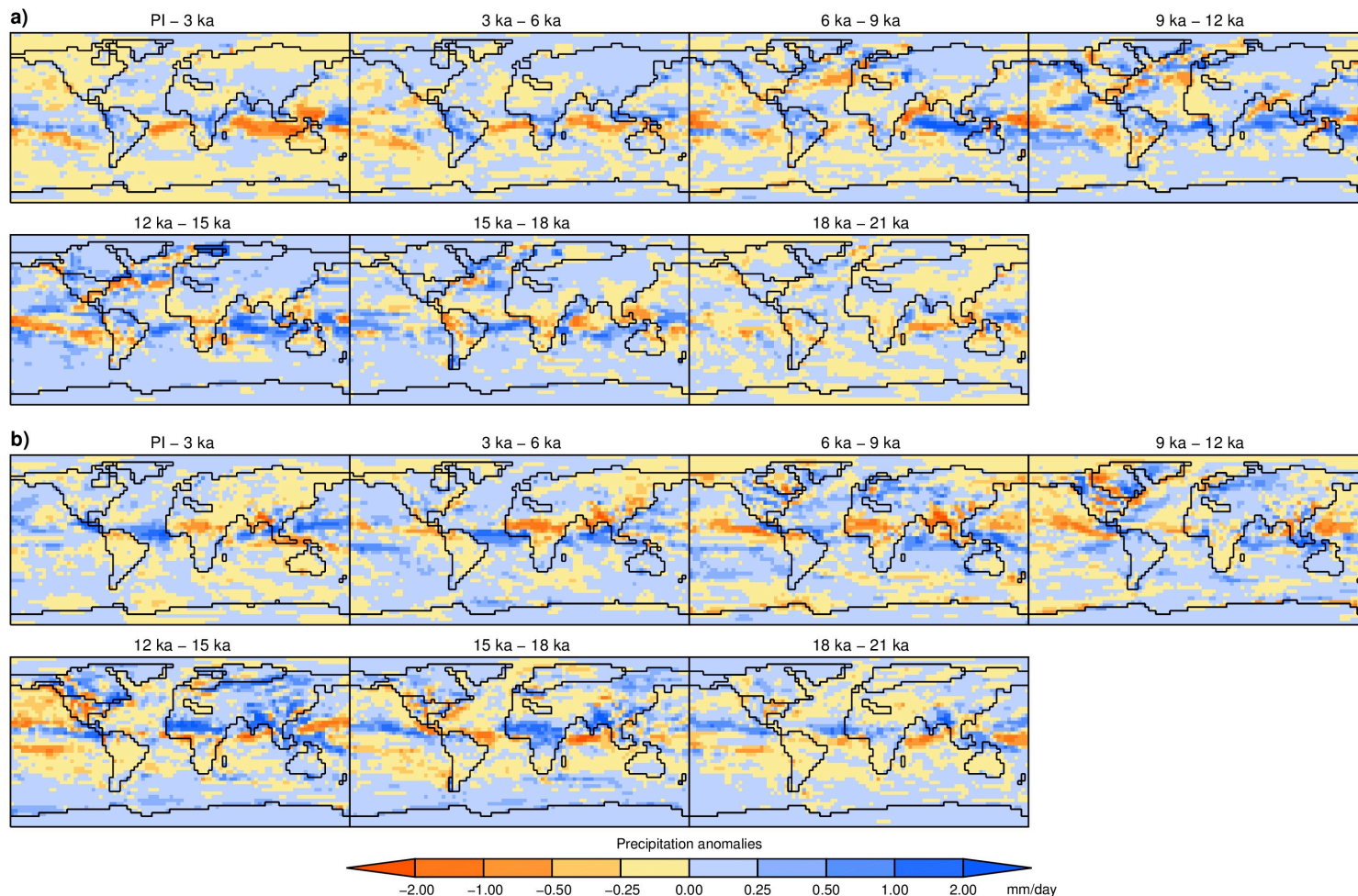
1212  
1213 Fig. 6. Simulated seasonal average 2-m air temperature anomalies relative to PI. a) December, January, and February and b) June,  
1214 July, and August.



1215  
1216 Fig. 7. Simulated seasonal average changes in 2-m air between consecutive time slices. a) December, January, and February and b)  
1217 June, July, and August.

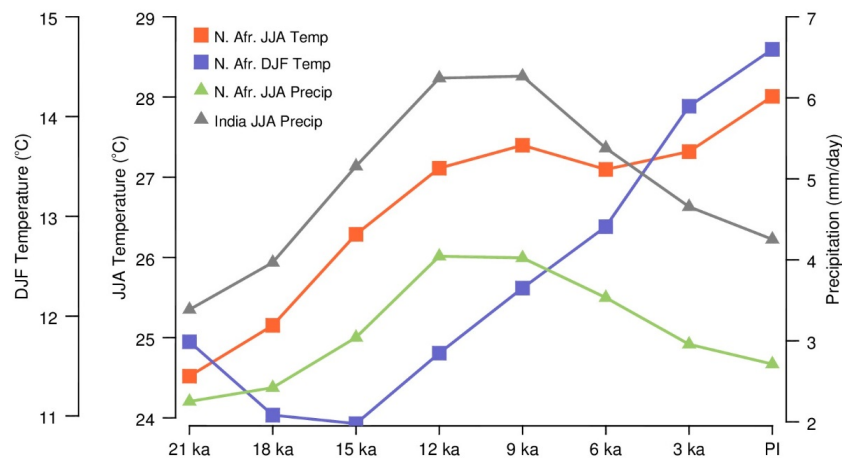


1218  
 1219 Fig. 8. Simulated seasonal average precipitation anomalies relative to PI. a) December, January, and February and b) June, July, and  
 1220 August.



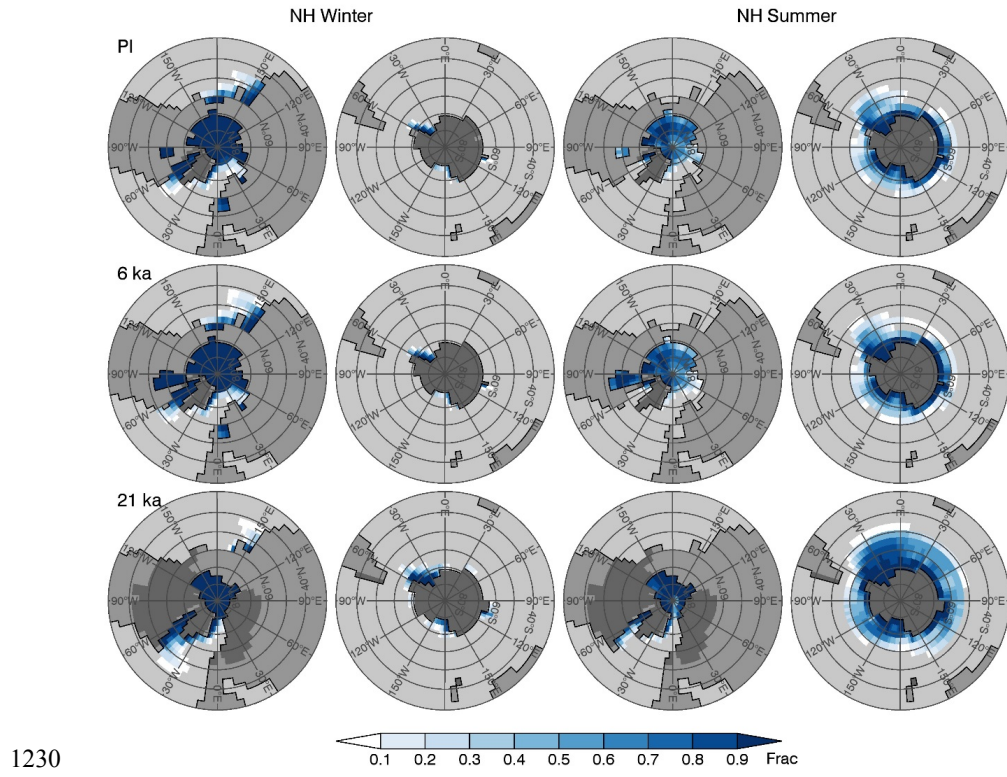
1221  
1222 Fig. 9. Simulated seasonal average precipitation changes between consecutive time slices. a) December, January, and February and b)  
1223 June, July, and August.

1224

1225  
1226

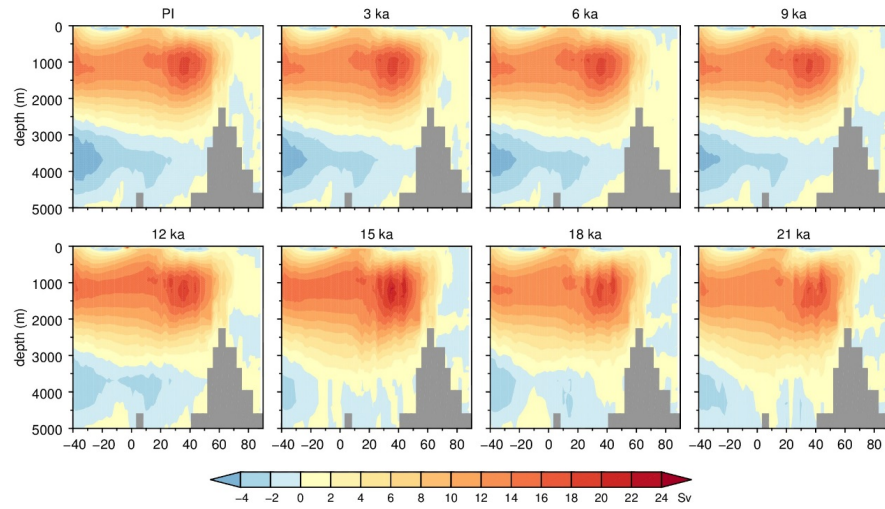
1227 Fig. 10. Time evolution of North African and Indian summer monsoons. The North  
 1228 Africa monsoon region is defined as 12°N - 30°N, 20°W - 30°E and India monsoon  
 1229 region is defined as 20°N - 40°N, 70°E - 100°E (Zhao and Harrison, 2012).

1230



1230  
1231 Fig. 11 Simulated sea-ice fraction for PI, 6 ka and 21 ka. Left two columns: February-  
1232 March and right two columns: August-September. Medium gray is continental land mass  
1233 and dark gray is continental ice sheet.

1234

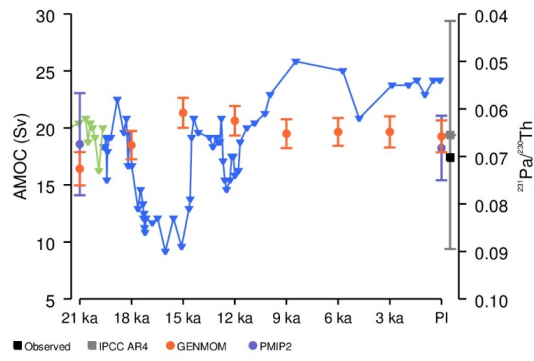


1234

1235 Fig. 12. Simulated annual average Atlantic Meridional Overturning Circulation (AMOC)

1236 for the eight time-slices.

1237



1237  
1238 Fig. 13. Simulated Atlantic Meridional Overturning Circulation (AMOC) compared to

1239  $^{231}\text{Pa}/^{230}\text{Th}$  proxy record at 33°N and other AOGCMs. Observations are from 26.5°N.

1240 GENMOM values are 100-yr averages with error bars representing standard deviations.

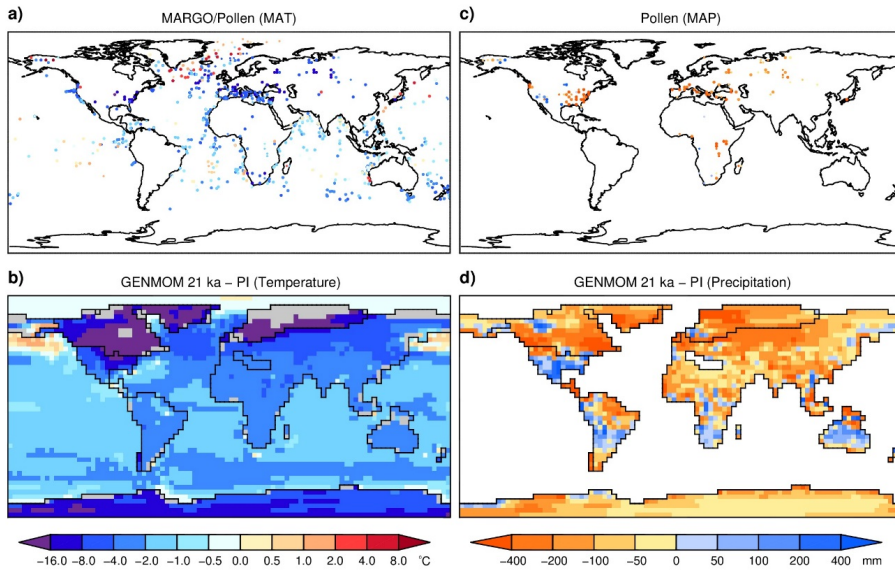
1241 The mean and standard deviation of the maximum AMOC in the five PMIP2 models. The

1242 IPCC AR4 point represents the mean and standard deviation from a collection of IPCC

1243  $^{231}\text{Pa}/^{230}\text{Th}$  data from McManus et al. (2004) and Lippold et al. (2009);

1244 observed value from Srokosz et al. (2012), PMIP2 data from Weber et al. (2007), and

1245 IPCC data from Schmittner et al. (2005).

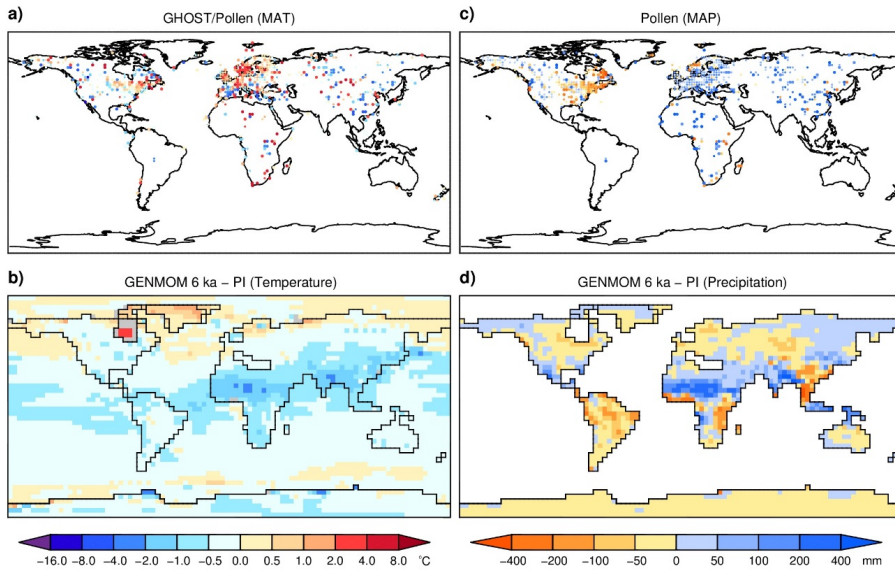


1246

1247 Fig. 14. Changes in 21 ka mean annual temperature (MAT) and precipitation (MAP)  
 1248 inferred from data and simulated by GENMOM. a) blended sea surface temperature from  
 1249 MARGO (Waelbroeck et al., 2009) and terrestrial temperature from Bartlein et al. (2011),  
 1250 b) GENMOM temperature anomalies (blended sea surface temperature and 2-m air  
 1251 temperature over land), c) precipitation from Bartlein et al. (2011), and d) GENMOM  
 1252 precipitation anomalies. Grid cells with different land mask types in the 21 ka and PI  
 1253 simulation are shaded in gray to avoid comparing ocean temperature to land temperature  
 1254 in emergent cells.

1255

1256



1256  
1257

1258 Fig. 15. Changes in 6 ka mean annual temperature (MAT) and precipitation (MAP)  
 1259 inferred from data and simulated by GENMOM. a) blended sea surface temperature from  
 1260 Leduc et al. (2010) and terrestrial temperature from Bartlein et al. (2011), b) GENMOM  
 1261 temperature anomalies (blended sea surface temperature and 2-m air temperature over  
 1262 land), c) precipitation from Bartlein et al. (2011) and d) GENMOM precipitation  
 1263 anomalies. Grid cells with different land mask types in the 6 ka and PI simulation are  
 1264 shaded in gray to avoid comparing ocean temperature to land temperature in emergent  
 1265 cells.  
 1266